ACS OMEGA

http://pubs.acs.org/journal/acsodf
Article

Distinguishing Nanoscale Electromechanical Properties in Hybrid Ferroelectric Systems: Insights from Bismuth Ferrite and PVDF-TrFE Flexible Nanocomposites

Pierre Nickmilder, Sergio González Casal, and Philippe Leclère*

Cite This: https://doi.org/10.1021/acsomega.6c01080
Read Online

ABSTRACT: The development of new electromechanically active materials has garnered significant attention in materials science, particularly in the pursuit of lead-free alternatives. Most current research focuses on macroscale characterization, leaving a gap in the understanding of nanoscale behavior, particularly the individual ferroelectric characteristics of complex hybrid systems. In this study, bismuth ferrite ($BiFeO_3$ or BFO) nanoparticles, successfully synthesized using a sol−gel method, are employed as a nanofiller to prepare polyvinylidene fluoride trifluoroethylene (PVDF-TrFE)-based ferroelectric nanocomposites. Advanced scanning probe microscopy (SPM) characterization techniques, including piezoresponse force microscopy (PFM), dual-frequency resonance tracking PFM (DFRT-PFM), switching spectroscopy PFM (ssPFM), and DataCube-PFM, are utilized to probe the nanoscale interactions and properties of the composite materials. The study reveals distinct ferroelectric behaviors in both components, with BFO exhibiting a clockwise hysteresis loop indicative of a positive piezoelectric coefficient, while the polymer displays a counterclockwise loop corresponding to a negative coefficient. Notably, some BFO regions show nonswitchable characteristics due to insufficient local polarization voltage. The apparent piezoelectric coefficients are quantified, showing consistent values for the polymer matrix and highly variable responses for the BFO aggregates. This research highlights the importance of nanoscale characterization in understanding the complex interactions within hybrid materials, thereby paving the way for future advancements in flexible electronics and energy-storage applications. The findings underline the necessity of comprehensive mapping of piezoelectric responses to guide the improved design and enhanced functionality of polymer-based nanocomposites.

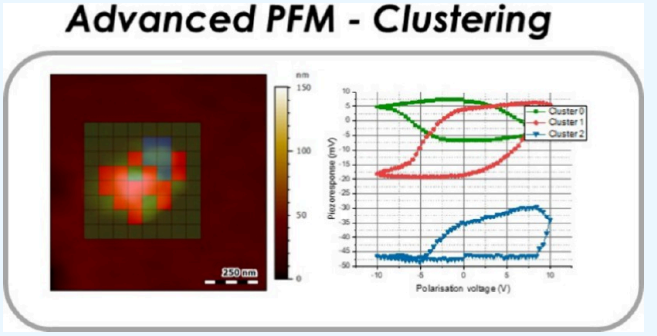

1. INTRODUCTION

The recent years have been highlighted by an energy crisis always more pressing, emphasizing the urgent need to shift toward alternative energy sources. Traditional fossil fuels and their negative environmental impacts have raised major concerns, triggering the development of cleaner and more sustainable energy options such as thermal, wind, vibrational, and solar energy.[1] Moreover, technological advancement in electronic device miniaturization and energy-efficient technologies has led to the creation of low-power systems operating with minimal energy consumption. For this reason, mechanical energy harvesting has emerged as a promising approach for powering low-power sensor networks and wearable electronics.[2,3] Piezoelectric apparatuses can be used to transform vibrational mechanical energy, ubiquitous in our environment, into electrical energy through the direct piezoelectric effect. Consequently, piezoelectric materials have garnered significant interest in recent years for the creation of piezoelectric harvesters.[4] Because of their straightforward design, they are easily integrated into sensors and other electronic devices.

Today, the most widespread piezoelectric materials are lead zirconium titanate (PZT) ceramics,[5] materials that exhibit strong piezoelectric response but that contain lead and raise concern regarding health and environmental safety with the risk of heavy-metal poisoning. The development of lead-free alternatives has become a significant focus within materials science.[6] The leading alternative candidates are barium titanate (BTO), potassium bismuth titanate (KBT), or bismuth ferrite ($BiFeO_3$ or BFO).[7] Among those, bismuth ferrite stand out as a well-known multiferroic material at room temperature.[8,9] This unique characteristic positions BFO as a promising component for various applications, including memory storage, sensors, and actuators.[10−12] However, the intricate processing requirements associated with ceramic materials often impede

Received: January 28, 2026
Revised: May 13, 2026
Accepted: May 20, 2026

their practical utilization.[13,14] To address this challenge, polymer-based nanocomposites have gained attraction, as they can retain the advantageous properties of BFO while simultaneously enhancing the attributes of the polymer matrix.[6,15,16] These composites present multiple advantages: lightweight architectures, corrosion resistance, flexibility, cost effectiveness, and ease of manufacturing.[17] Polyvinylidene fluoride (PVDF) and its copolymers as the structural matrix of nanocomposites have attracted a lot of interest due to their intrinsic piezoelectric, pyroelectric, and ferroelectric properties.[18−20]

The integration of BFO nanoparticles within a PVDF polymer matrix results in a composite material exhibiting improved functional properties and broadening its applicability in piezoelectric, ferroelectric, dielectric and mechanical energy harvesting devices, as well as in self-powered electronic systems.[21−24] Research on PVDF/BFO composites have further expanded well beyond simple piezoelectric harvesting or sensor devices. Several studies highlight the multifunctionality of such composites, as multistimuli-responsive materials for energy harvesting and catalysis,[25] or anticorrosion properties,[26] and as a decomposing agent for salt in lithium battery.[27]

Even though a large portion of the research carried out on these systems focuses on macroscopic characterization,[21,28,29] very few take into consideration the nanoscopic characterization. The nanoscopic nature of these systems underscores the critical importance of understanding interfacial and local electromechanical behaviors at the nanoscale, where polymer−nanoparticle interactions, phase distribution, and local domain configurations can strongly influence the macroscopic performance. Understanding interactions at the nanoscale can provide insights into the mechanisms driving the enhanced properties, ultimately guiding future material design and engineering efforts.

The invention of atomic force microscopy (AFM) made it possible to characterize the material properties at the microscopic scale. After decades of extensive development, the functions of AFM have been greatly expanded, capable of interrogating a wide range of localized phenomena, ranging from mechanical[30,31] to electrical.[32,33] Among these, piezoresponse force microscopy (PFM)[34] has emerged as a powerful tool to measure weak piezoelectric displacement. This mode has risen as a robust technique for the detailed characterization of surface properties at this scale, especially for energy harvesting.[34,35] It is used on different systems for a global ferroelectric assessment.[15,36,37] Some other studies have used the high spatial resolution of this mode to try access different responses in composite systems on single localization.[38,39] Nevertheless, no study has shown a complete cartography of the different ferroelectric structures and properties inside both phases of this kind of complex system simultaneously.

However, the quantification of surface displacement arising from piezoelectric effect at the nanoscale is an ongoing debate in the PFM community. Even though some studies have used a PFM setup mimicking macroscale measurement to evaluate the piezoelectric coefficient,[40−43] the presence of numerous parasitic signals intrinsic to PFM tends to question the reliability of these results. These include electrostatic forces, surface electrochemical effects, electrostriction, Joule heating, and flexoelectric contributions.[44]

Among these factors, electrostatic interactions are generally considered the most significant source of artifacts as they may even dominate the measured signal under certain conditions. Electrostatic forces arise from the interaction between the charged probe and the surface potential of the sample, which can induce a cantilever deflection without any actual surface displacement. As a result, the measured response may reflect only the intrinsic piezoelectric behavior of the material.

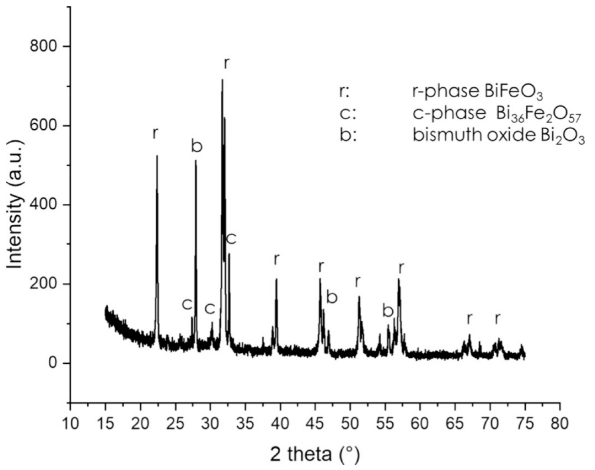

Figure 1. X-ray diffraction spectrum of BFO particles synthesized using the sol−gel method.

To minimize these contributions, several experimental precautions were typically implemented. These include operating at relatively low excitation voltages and ensuring stable mechanical contact by using stiff cantilevers and sufficiently high contact set points. In addition, a practical approach reported in the literature to reduce the sensitivity of the measurement to electrostatic effects consists of optimizing the optical beam deflection (OBD) detection system at the electrostatic blind spot (ESBS) position.[45]

Such precautions are essential to ensuring that the apparent surface displacement measured by the PFM setup remains as close as possible to the true piezoelectric surface displacement.

Different approaches are to extract piezoelectric coefficients from PFM measurements, including extracting surface displacement from PFM images,[46] converting amplitude or piezoresponse loops, either on-field[15,47,48] or off-field,[43] and determining the slope of amplitude versus V_{ac} at selected locations.[37,49,50] Among these techniques, fixed-position measurements are generally regarded as the most reliable, as they minimize topographic crosstalk, while the force-spectroscopy approach provides improved mechanical stability during the measurement. Since ssPFM inherently acquires data at a fixed tip location and includes single harmonic oscillator (SHO) fitting of the piezoresponse, converting ssPFM data is a straightforward and robust approach to estimate the apparent displacement.

This study aims to present a methodology for the characterization of complex hybrid ferroelectric systems by PFM to distinguish and attribute the electromechanical properties of each constitutive component of the hybrid material, broadening the range of nanoscale interaction comprehension. Thin films of the PVDF-TrFE/BFO nanocomposite are prepared by spin coating. Samples of isolated constituents were also prepared following the same procedure for the sake of comparability. BFO particles are synthesized following a sol−gel process. The polymer and BFO were spin-coated together on top of conductive indium tin oxide (ITO)

https://doi.org/10.1021/acsomega.6c01080
ACS Omega XXXX, XXX, XXX−XXX

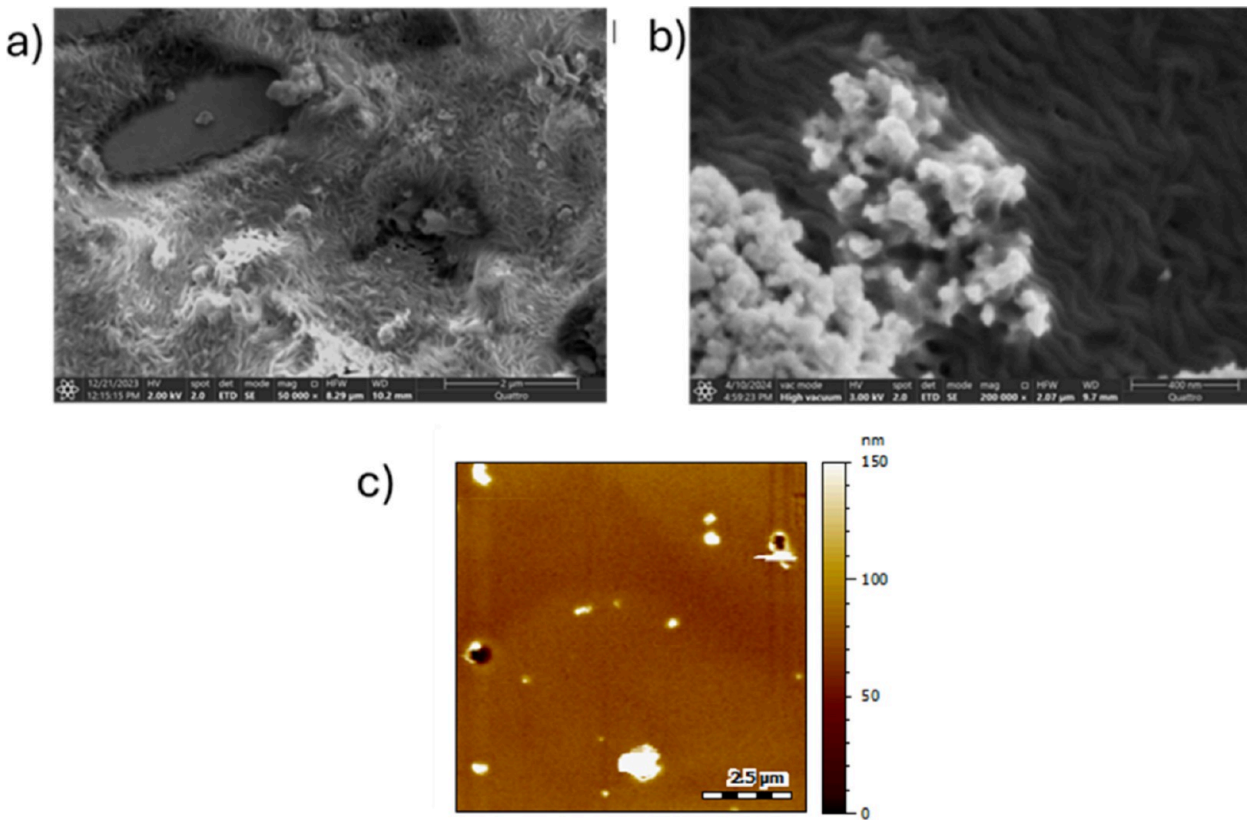

Figure 2. (a, b) eSEM images of BFO−PVDF-TrFE nanocomposites prepared by spin coating. (c) Peak force tapping topographic image of the same sample.

substrates. The local properties are investigated using various scanning probe microscopy (SPM) techniques focusing on piezoresponse force microscopy mode (PFM) and its derivatives[51] including switching spectroscopy PFM (ssPFM) for more precise ferroelectric evaluation. ssPFM data analysis is carried out with the help of PyssPFM software.[52] The evaluation of the dynamic surface displacement distribution is based on a spectroscopic mapping reconstruction facilitated by the DataCube-PFM mode from Bruker.[53]

2. MATERIALS AND METHODS

2.1. Sample Preparation

2.1.1. BFO Powder Synthesis. The sol−gel method was used to prepare $BiFeO_3$ particles.[16] A precursor solution was prepared by mixing an equimolar proportion of bismuth nitrate pentahydrate [$Bi(NO_3)_3{\cdot}5H_2O$] (Aldrich) with iron nitrate nonahydrate [$Fe(NO_3)_3{\cdot}9H_2O$] (Aldrich) in ethylene glycol. The solution was stirred for 2 h at 80 °C. The reddish solution was dried at 150 °C for half an hour until the formation of a yellowish gel. This powder was annealed at 600 °C for 1 h in an N_2 atmosphere in a furnace. These conditions are known to favor the synthesis of the ferroelectric rhombohedral phase of BFO.[54] The resulting powder was ground inside a mortar before being leached with diluted nitric acid (1 M) to remove phase impurities. The final powder was washed with distilled water eliminated by a centrifugation process. Crystal structures of BFO powder were investigated by X-ray diffraction (XRD; Bruker D5000). The crystal structure of the BFO powder was investigated by X-ray diffraction (XRD). Measurements were performed using a Panalytical Empyrean diffractometer equipped with a Cu Kα radiation source (λ_1 = 1.54056 Å and λ_2 = 1.54443 Å) and a PIXcel1D (RTMS) detector. The diffraction patterns were used to determine the crystalline phases of the BFO particles, and the reflections were assigned to the rhombohedral $BiFeO_3$ phase (JCPDS No. 71-2494).

2.1.2. Thin-Film Preparation. Pure PVDF-TrFE thin films were prepared using a 5 wt % solution of PVDF-TrFE 70:30 (Piezotech, Arkema) dissolved in a DMF−acetone (2/3−1/3) mixture (Aldrich). This solution was magnetically stirred for several hours to ensure complete dissolution of the polymer. The samples were then spin-coated at 4000 rpm for 30 s with an acceleration of 300 rpm/s onto conductive ITO-coated glass substrates (R = 70−100 Ω/sq, Aldrich). The substrates were previously cleaned in an RBS bath, rinsed with distilled water, and dried under N_2 flux.

PVDF-TrFE/BFO composite thin films were fabricated using the same polymer solution (5 wt %), with the addition of BFO powder to obtain a composite containing 5 wt % BFO relative to PVDF-TrFE. This proportion produced relatively small and well-dispersed particle aggregates in the matrix.[16] The mixture was sonicated to achieve a uniform dispersion of the particles prior to spin coating onto ITO substrates. The same spin-coating parameters as those for the pure PVDF-TrFE films were used.

BFO particles were also prepared as composites embedded in a conductive polymer matrix. This matrix served to mechanically stabilize the particles during AFM measurements while ensuring an electrical connection between the polymer and the ITO surface. An aqueous solution of poly(3,4-ethylenedioxythiophene) polystyrene-sulfonate (PEDOT:PSS) was chosen for this purpose. BFO powder was added to reach 0.25 wt %, and the mixture was sonicated to ensure uniform dispersion of the particles before spin coating onto ITO substrates.

All thin-film samples were annealed at 140 °C for 2 h, with a heating and cooling rate of 1 °C/min. For the PVDF-TrFE-based films, annealing at this temperature increases the proportion of the β-crystalline phase (Figure S1),[55] thereby enhancing the intrinsic ferroelectric properties of the polymer.[56,57] For the PEDOT:PSS-based films, annealing at this temperature decreases the resistivity of PEDOT:PSS.[58]

No supplementary poling procedure was necessary to observe ferroelectric domains in the PVDF-TrFE films. Film thicknesses were

https://doi.org/10.1021/acsomega.6c01080
ACS Omega XXXX, XXX, XXX−XXX

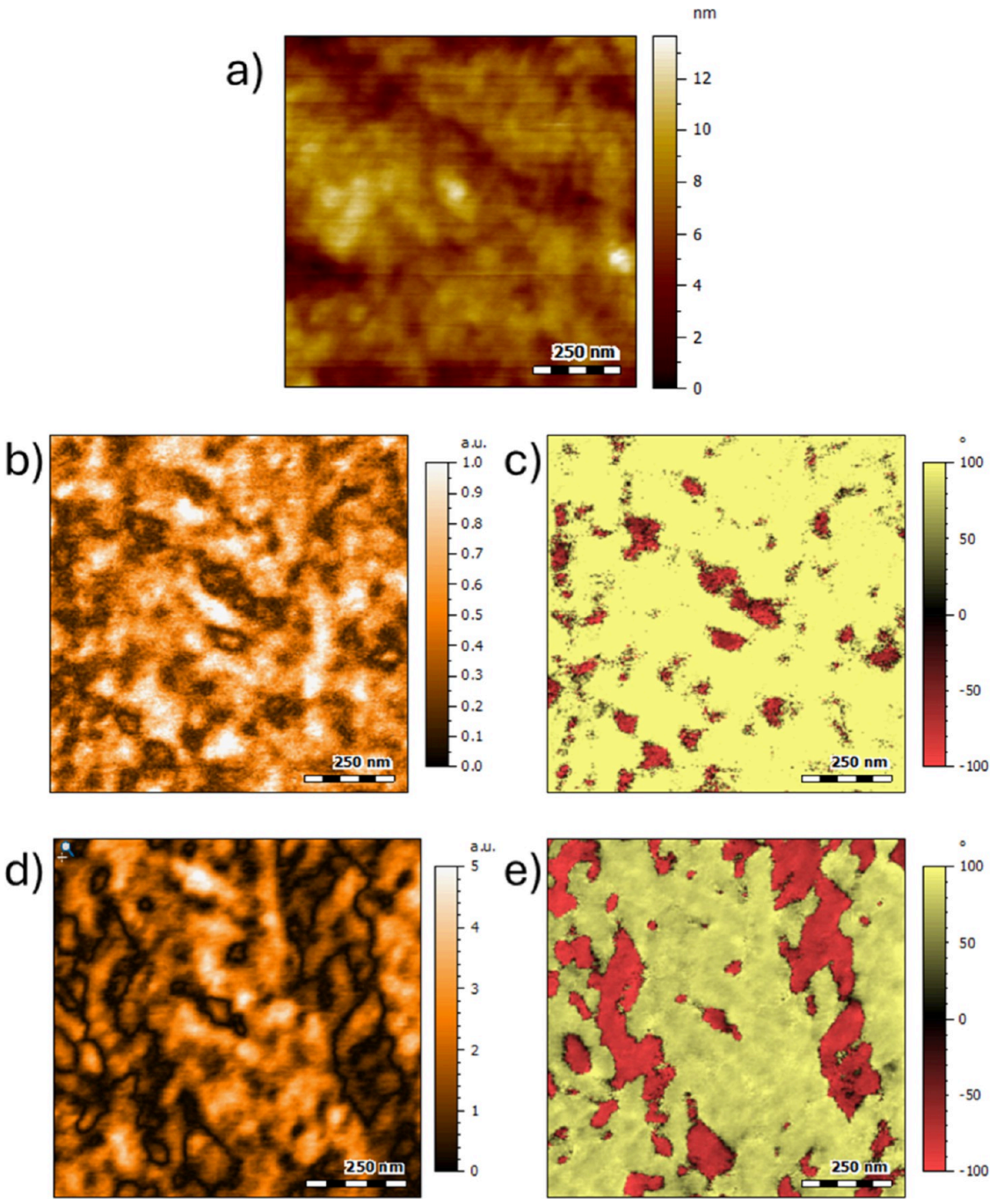

Figure 3. DFRT-PFM imaging of the PVDF−TrFE film. Vertical mode (CR frequency 250−350 kHz): (a) topography, (b) amplitude, and (c) phase. Lateral mode (CR frequency 600−800 kHz): (d) amplitude and (e) phase.

measured using an AFM scratch test (Figure S2). The film thickness was evaluated to be between 20 and 60 nm depending on the region.

2.2. Nanoscale Measurements

All atomic force microscopy (AFM) measurements were performed using a Dimension Icon AFM (Bruker Nano Inc., Santa Barbara, California, USA). Data were analyzed using Nanoscope Analysis 3.0 (Bruker, Santa Barbara, USA) and Mountains 11.1 (DigitalSurf, Besançon, France) software. Electrical contact was established between the conductive AFM tip (top electrode) and the ITO-coated glass substrate (bottom electrode), with a metallic pin connecting an exposed area of the ITO to the AFM circuitry.

Local mechanical properties were assessed using PeakForce Quantitative Nanomechanical Mapping (PF-QNM). Measurements employed RTESPA-300 cantilevers (Bruker Nanoprobes), nominal spring constant ≈40 N/m, tip radius <10 nm. Deflection sensitivity and effective spring constant were calibrated on a rigid sapphire reference (Figure S3). Indentation depths of a few nanometers were achieved by setting an oscillation amplitude of 40 nm, a scan rate of ∼0.4 Hz, and a force set point of 50 nN. Images were collected at 256 × 256 or 512 × 512 pixel resolution.

Local conductivity was measured using conductive AFM (C-AFM) with PFTUNA probes (Bruker Nanoprobes) (spring constant ≈ 0.4 N/m). A current preamplifier enabled detection in the picoampere range. Full I−V maps were acquired (32 × 32 or 64 × 64 pixels) with a set point of 20 nN and a hold time of 50 ms per point, to assess potential electrical breakdown in the studied polarization range (−10 to 10 V).

https://doi.org/10.1021/acsomega.6c01080
ACS Omega XXXX, XXX, XXX−XXX

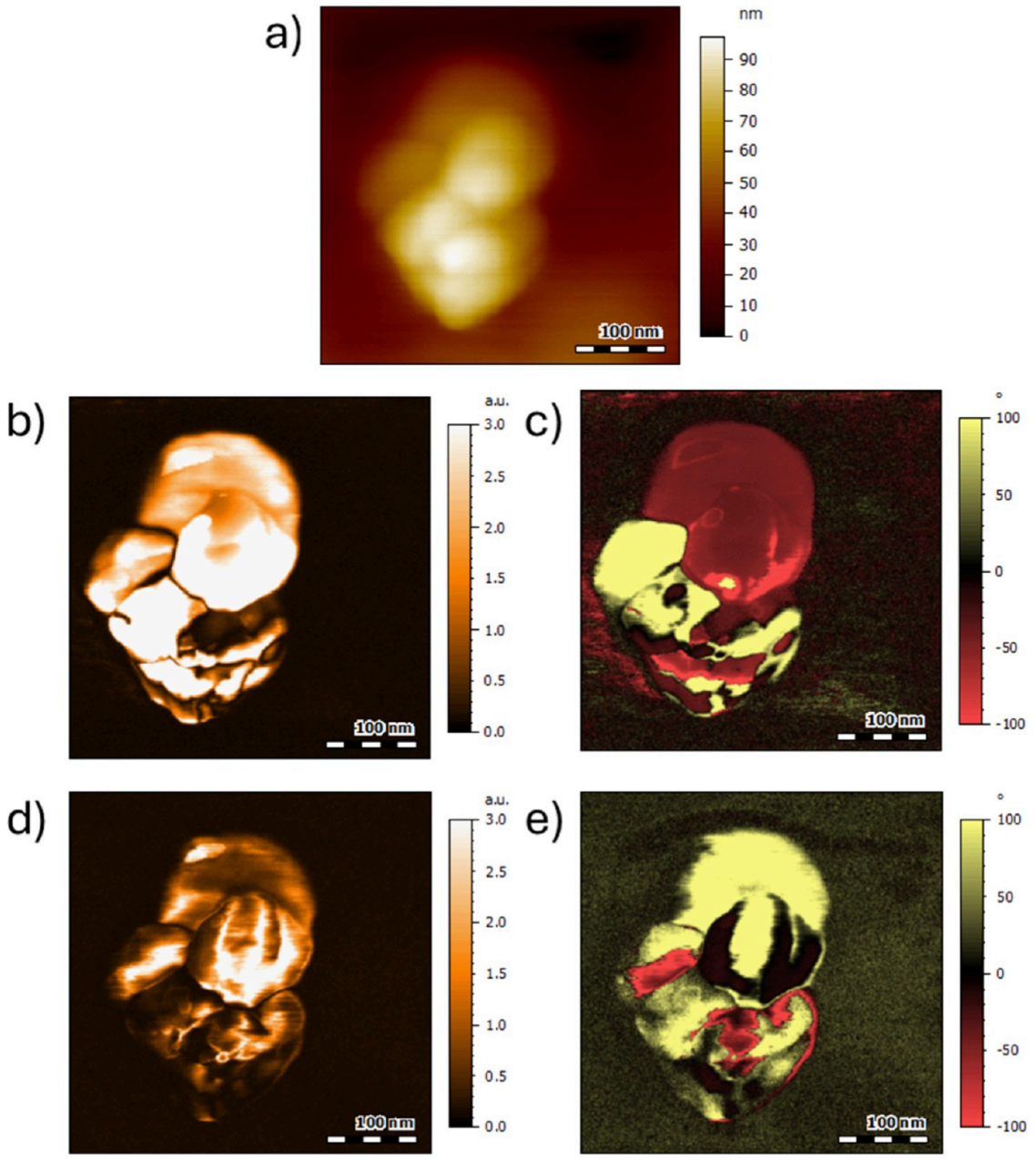

Figure 4. DFRT-PFM imaging of a BFO aggregate in the PEDOT:PSS matrix. Vertical mode (250−350 kHz): (a) topography, (b) amplitude, and (c) phase. Lateral mode (600−800 kHz): (d) amplitude and (e) phase.

Piezoelectric and ferroelectric responses were investigated using piezoresponse force microscopy (PFM).[59] SCM-PIT-V2 tips (Bruker Nanoprobes) (spring constant 3 N/m) were used for all PFM modes, with a set point force of 50 nN. Measurements included vertical (VPFM) and lateral (LPFM) responses in contact-resonance mode.[60] Resonance frequencies ranged from 200 to 350 kHz (vertical) and from 600 to 800 kHz (lateral). Unless stated otherwise, the probing voltage for all measurements was set at 1 V. Prior to measurement, the tip was mechanically calibrated in the same manner as for PF-QNM. To minimize the electrostatic noise contribution to the signal, the laser was aligned at the electrostatic blind spot (ESBS) (Figure S4),[45] and phase calibration was performed using a PZT reference with well-defined ferroelectric domains (Figure S5).[61]

PFM imaging was performed in dual-frequency resonance tracking (DFRT) mode, with a Zurich HF2LI lock-in amplifier (Zurich Instruments, Zurich, Switzerland) enabling real-time resonance tracking during imaging. DFRT-PFM images were collected at 256 × 256 or 512 × 512 pixels, in both vertical and lateral modes.[62]

Ferroelectric switching was characterized using switching spectroscopy PFM (ssPFM).[51] In this mode, hysteresis curves were reconstructed from a series of polarization (on-field) and non-polarization (off-field) voltage steps while continuously recording the piezoresponse. Each measurement consisted of 10 loop cycles, each containing 50 steps (Figure S6). Each step involved a frequency sweep with a single harmonic oscillator (SHO) fit applied to extract amplitude, phase, and quality factor. The data are extracted following the Lorentzian model coupled with symmetric least-square fit (Figure S7). Data are presented as mean loops across the cycles. ssPFM data were collected as grids (4 × 4 up to 10 × 10), analyzed using PyssPFM software,[52] which incorporates a clustering option to visualize the main behavior in each cluster. Both on-field and off-field results were used to verify the ferroelectric nature of the signal. Supplementary single-position measurements at different reading voltage V_{dc0} values were also performed to reconstruct contact Kelvin probe force microscopy (cKPFM) data for further confirmation.[63,64] The presence of two stable states at reading polarization voltage

https://doi.org/10.1021/acsomega.6c01080
ACS Omega XXXX, XXX, XXX−XXX

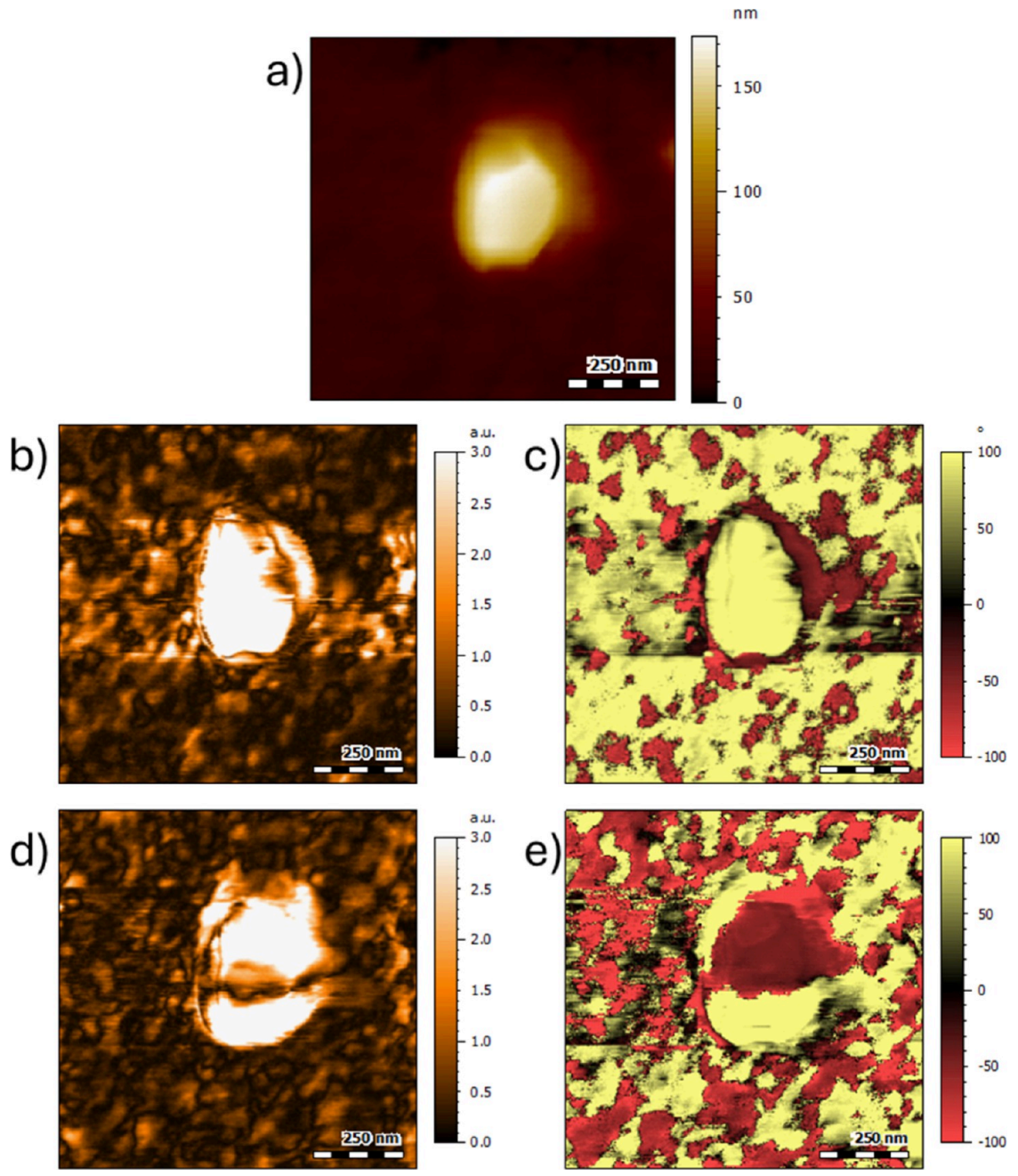

Figure 5. DFRT-PFM imaging of an isolated BFO particle embedded in PVDF−TrFE. Vertical mode (250−350 kHz): (a) topography, (b) amplitude, and (c) phase. Lateral mode (600−800 kHz): (d) amplitude and (e) phase.

exceeding the positive and negative coercive fields is used as a criterion for ferroelectric behavior. Conversely, the absence of such bistability indicates a nonferroelectric or nonswitchable response (Figure S8). These verifications are illustrated on known ferroelectric and nonferroelectric samples in Figure S9.

Different approaches exist to extract piezoelectric coefficients from PFM measurements, including extracting surface displacement from PFM images,[46] converting amplitude or piezoresponse loops, either on-field[15,47,48] or off-field,[43] and determining of the slope of amplitude versus V_{ac} at selected locations.[37,49,50] Among these techniques, fixed-position measurements remain the most reliable as they avoid topographic crosstalk. Since ssPFM inherently acquires data at a fixed tip location and includes SHO fitting of the piezoresponse, converting ssPFM data is a straightforward and robust approach to estimate the apparent displacement.

Local apparent d_{33} evaluations (d_{33app}) were collected on preidentified regions of interest. Successive SHO measurements were performed after local polarization.[61] Using the ssPFM function with zero-polarization voltage, thousands of SHO fits could be collected in a single measurement, while reducing the presence of electrostatic forces. Apparent surface displacement D was extracted from SHO data using the following equation: $D = V_{ac} \times A \times Q \times \sin(\phi)$, where A is the amplitude, Q the quality factor, ϕ the phase, and V_{ac} the probing voltage. The use of the sine function instead of the cosine arises from the phase convention adopted in this study, where the up and down polarization states are defined at −90 and +90°, respectively. This choice minimizes potential phase overshoot effects during the measurements.

d_{33app} was determined from the linear regression of D as a function of V_{ac}. For each voltage step, the distribution of D values remains

https://doi.org/10.1021/acsomega.6c01080
ACS Omega XXXX, XXX, XXX−XXX

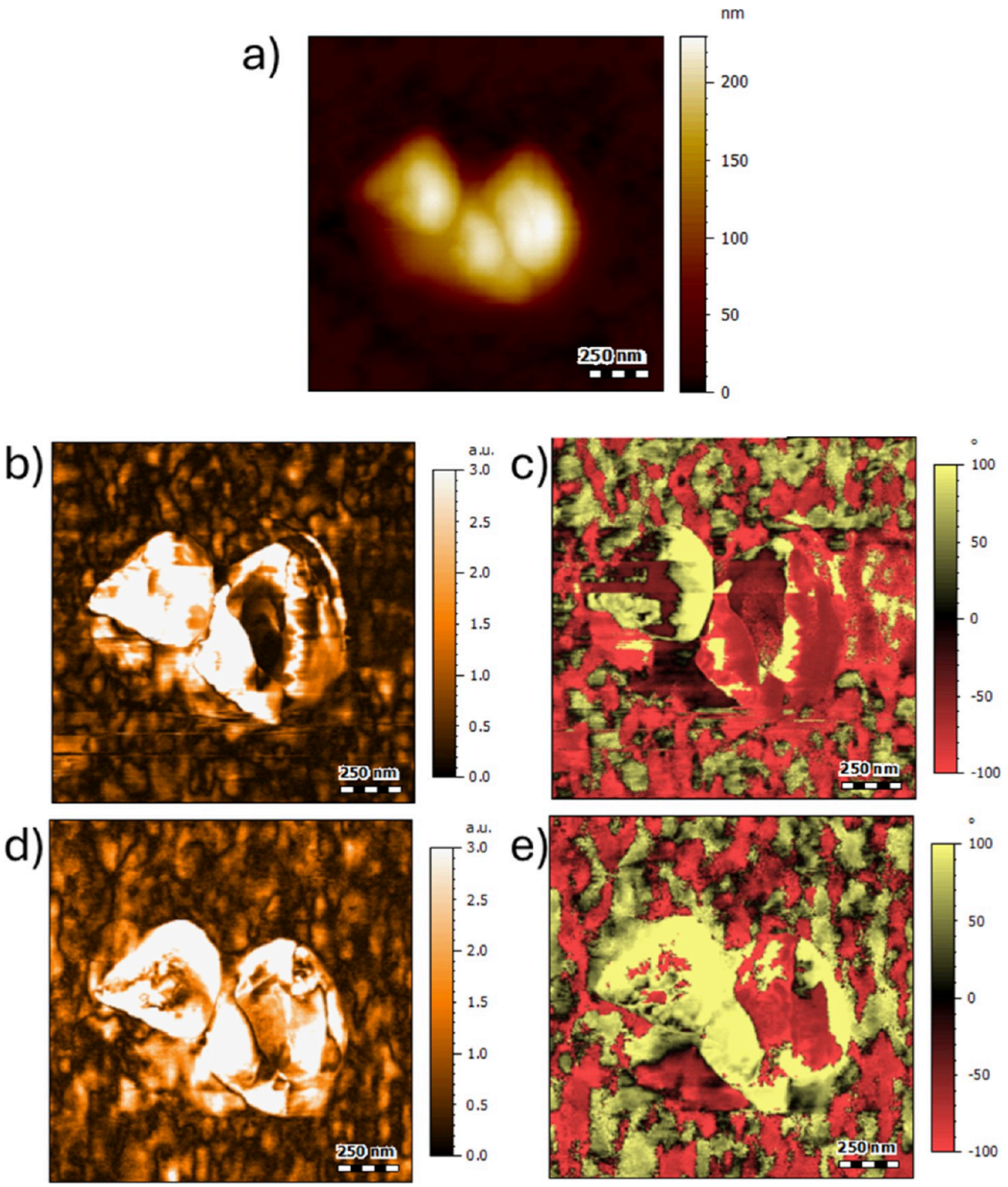

Figure 6. DFRT-PFM imaging of a multigrain BFO aggregate embedded in PVDF−TrFE. Vertical mode (250−350 kHz): (a) topography, (b) amplitude, and (c) phase. Lateral mode (600−800 kHz): (d) amplitude and (e) phase.

consistent, with a typical standard deviation below 10% of the mean value, as shown in Figure S10.

The distribution of apparent surface displacement across samples was further investigated using DataCube-PFM (DataCube-PFM or FFV PFM).[53] In this spectroscopic mode, force curves were collected at each pixel, maintaining a short contact period (30 ms), during which a frequency sweep was applied. The resulting parameter maps allowed reconstruction of D as well as access to local mechanical parameters such as adhesion and local contact resonance.

To ensure consistency between measurements, each probe was calibrated using a reference material with a well-established d_{33} value. A ZnO thin film with a known piezoelectric coefficient (d_{33} = 5.8 ± 1.3 pm/V), previously determined by interferometric measurements, was used as the reference sample (Figure S11a). The apparent piezoelectric coefficients measured in this study were normalized using a correction factor derived from preliminary measurements performed on the ZnO reference film (Figure S11b), allowing comparison between different probes and measurement sessions.

3. RESULTS AND DISCUSSION

3.1. X-ray Diffraction

The X-ray diffraction pattern of the sol−gel synthesized BFO powder is presented in Figure 1. The main phase readily identified is the rhombohedral (R-phase), which is the main ferroelectric phase of the $BiFeO_3$ perovskite. Besides the formation of the main BFO R-phase, some remanent traces of cubic phase BFO ($Bi_{36}Fe_{24}O_{57}$) and bismuth oxide (Bi_2O_3) are detected from the XRD analysis after the different cleaning procedures.

https://doi.org/10.1021/acsomega.6c01080
ACS Omega XXXX, XXX, XXX−XXX

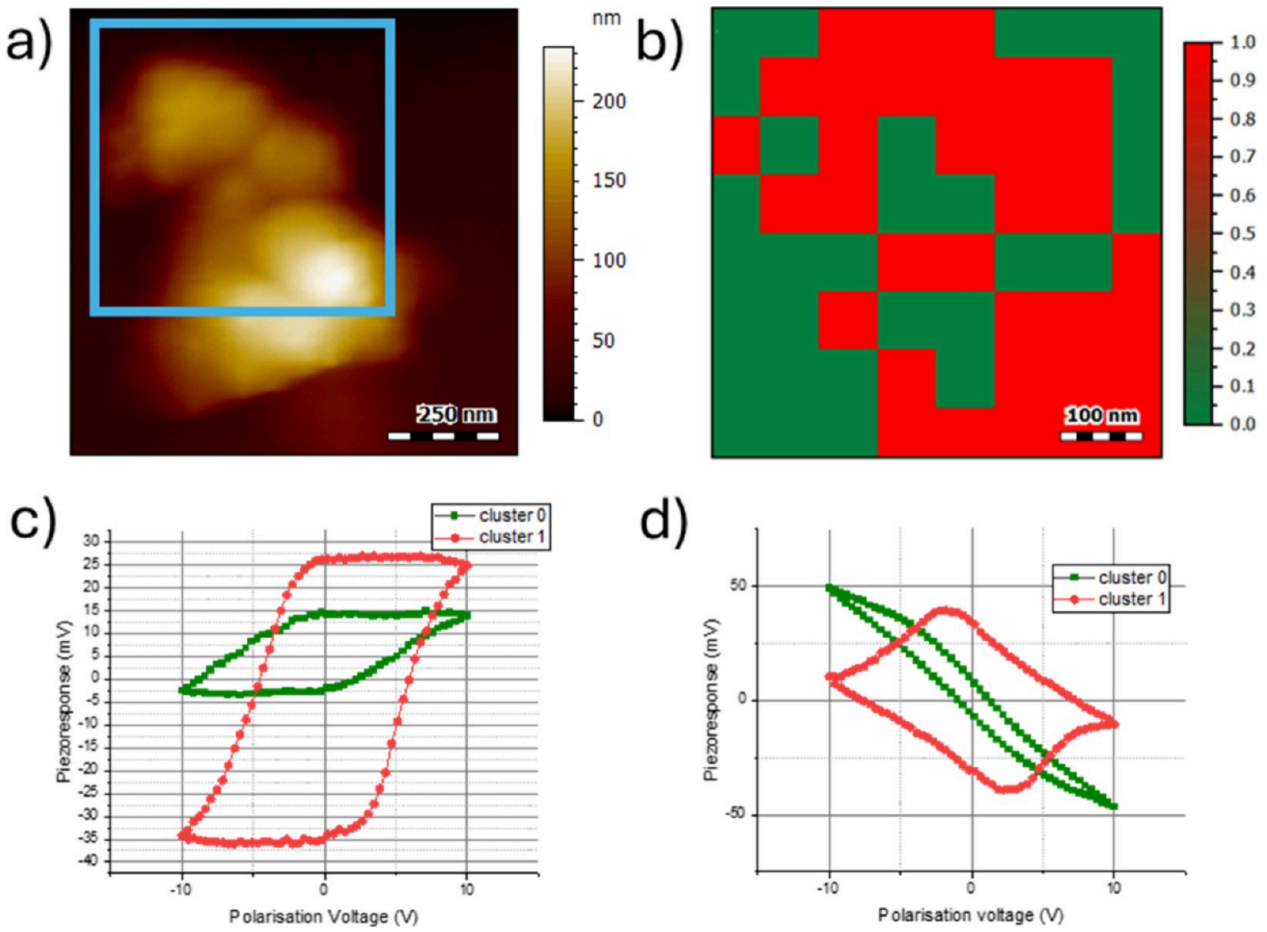

Figure 7. (a) Topography of BFO aggregates. The blue square marks the region used for ssPFM mapping (8 × 8 curves over 500 × 500 nm).(b) PyssPFM clustering for k = 2. (c) Mean off-field piezoresponse loops. (d) Mean on-field piezoresponse loops.

3.2. Morphology

Typical environmental scanning electron microscopy (eSEM) images of the nanocomposite samples are presented in Figure 2. The polymer matrix is easily identifiable from its fibrillar "Rice-like" structuration, which arises when the system is annealed at 140 °C.[65] The same type of observation is reported on the pure PVDF-TrFE thin film (Figure S12a). BFO particles are dispersed in form of aggregates of variable size, embedded inside the polymer. Many of those particles exhibit an exposed, polymer-free surface on the z-axis, which is suitable for PFM measurements. Although the film is considered macroscopically homogeneous, some small variations are locally observed. On the left top size, one can observe areas where the ITO substrate surface becomes visible, probably arising from the rearrangement of the polymers during drying or from particle ejection during the spin-coating process.

From Figure 2b, the actual size of the particles can be estimated to be around 50−150 nm, as expected with this synthesis route. Even though many larger aggregates are observed inside the structure aggregates, single particles trapped inside the polymer can also be seen. The same kind of observations are made for the BFO trapped in the PEDOT:PSS sample (Figure S12b).

Local scratch test on the nanocomposite revealed a thickness variation of the polymer between 20 and 60 nm. Complementary, C-AFM measurements for both the polymer (Figure S13) and the particles (Figure S14) in the studied voltage range (±10 V), indicating that all measurements are performed without risk of electrical breakdown. A summary table of the different sample thickness, surface roughness, and typical exposure of studied BFO aggregates is presented in Figure S15.

3.3. DFRT-PFM Imaging

DFRT-PFM imaging of the PVDF-TrFE thin films is presented in Figure 3. Both the vertical and lateral results are presented. The sample exhibits ferroelectric domain structures in both imaging modes, without any prior poling. These maps reveal randomly distributed polarized domains with elongated shapes, 10−50 nm in width and extending over several hundred nanometers. No relation is observed between the orientation of the in-plane (Figure 3b,c) and out-of-plane domains (Figure 3d,e), nor between either of those with the topography. The presence of ferroelectric domains in both in-plane and out-of-plane orientations in PVDF-TrFE was reported previously.[66]

The same kind of distribution of the ferroelectric domains is observable on the BFO particles. Figure 4 focuses on half-micrometer-wide BFO aggregates embedded in the PEDOT:PSS matrix. Notable variations in the response are observed. Regions corresponding to the polymer matrix are identified as nonactive, corresponding only to amplitude walls in the visible phase domain structure, while some phase changes are observable on larger particles without the corresponding amplitude walls. These most likely arise from

https://doi.org/10.1021/acsomega.6c01080
ACS Omega XXXX, XXX, XXX−XXX

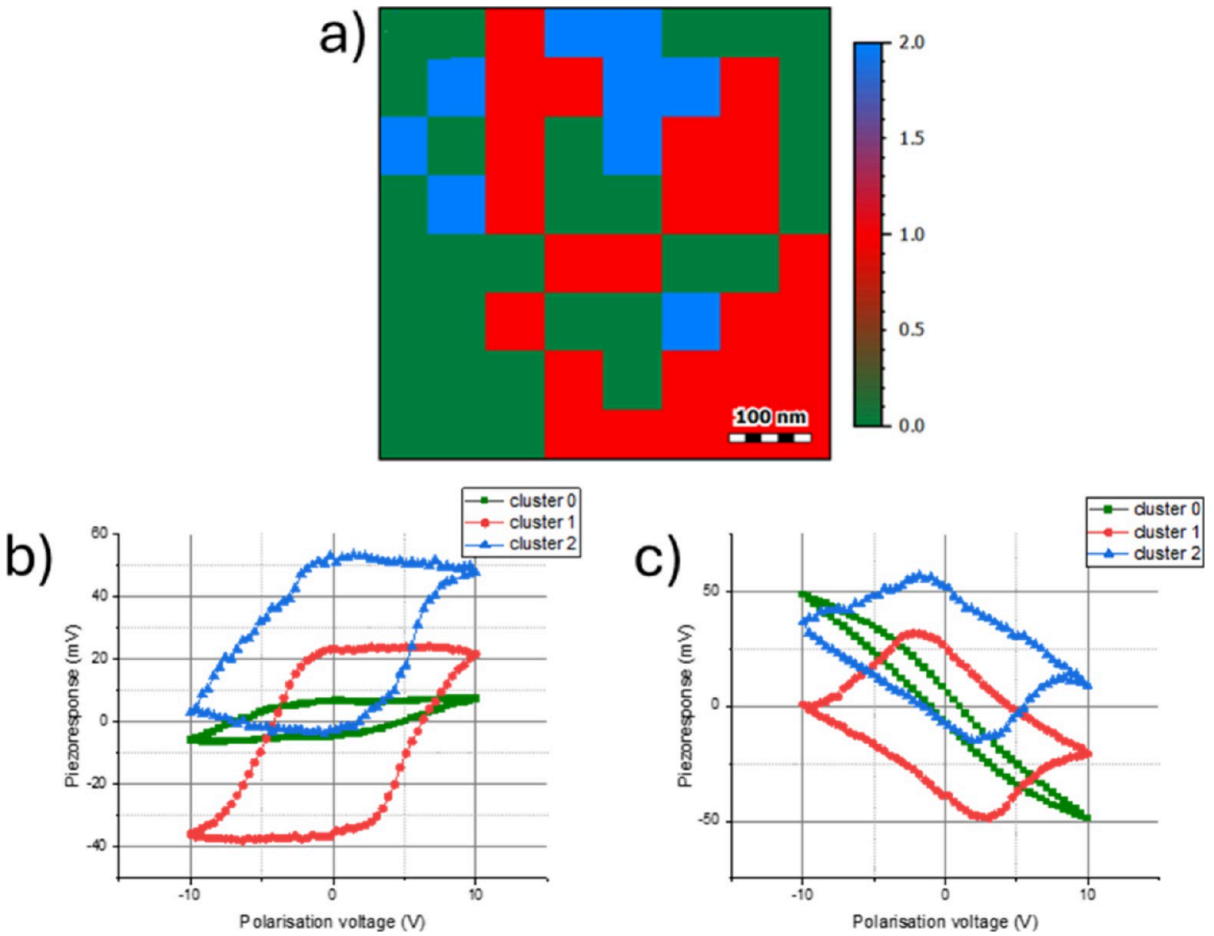

Figure 8. (a) PyssPFM clustering of the same region as Figure 7 for $k = 3$. (b) Mean off-field piezoresponse loop. (c) Mean on-field piezoresponse loop.

phase flips during the measurement because the DFRT-PID gain does not have enough time to perform proper tracking.

Figure 5 presents results for the hybrid ferroelectric nanocomposites, focusing on an isolated particle. The vertical and lateral PFM responses, in both amplitude and phase, are consistent with those observed for the corresponding isolated components.

Bigger BFO clusters show the same disparity of measurement on the particles Figure S16. Some domains in phase images do not present their counterparts in amplitude images (Figure 6). Those "domains" changes with the scan direction (Figure S17). Increasing the phase scale reveals that they exceed the normal phase limitation (±90°) confirming there are artifactual flip, likely originating from the mechanical and roughness variation of the sample.

To our knowledge, no study has presented images showing simultaneous ferroelectric domains of both components inside a ferroelectric nanocomposite. The mechanical difference between the filler and the matrix (Figure S18) leads to an important difference of resonance frequency between the two components (Figure S19), limiting the use of the conventional PFM technique. These findings highlight the critical importance of resonance frequency tracking for PFM imaging, particularly in samples with significant disparities in the mechanical properties. Although DFRT constitutes an improvement over conventional PFM, it remains sensitive to rough surface contact conditions, as present in any SPM measurement, limiting measurement stability.

3.4. ssPFM

The distribution of ferroelectric properties is further investigated using ssPFM. Each ssPFM measurement consists of 10 consecutive cycles, of which 9 are averaged. The first cycle is systematically discarded, as it corresponds to the initial unpoled state of the system (Figure S20). Both on-field and off-field data are recorded for each measurement. The data are acquired as X−Y grids of piezoresponse curves over defined spatial areas, enabling spatially resolved analysis. The piezoresponse loops within each grid are analyzed using a *K*-means clustering algorithm, which classifies the data based on distinct loop characteristics. A representative mean curve is then generated for each cluster.

The ferroelectric response distribution in the BFO-in-PEDOT:PSS samples is shown in Figure 7. The polymer matrix and BFO aggregates are readily identified from the topographic image (Figure 7a). When the data set is processed using PyssPFM with a fixed number of clusters ($k = 2$), the clustering clearly separates the two phases: cluster 0 corresponds to PEDOT:PSS and cluster 1 to BFO (Figure 7b). The BFO regions exhibit the expected well-defined ferroelectric hysteresis loops in off-field measurements (cluster 1).

Interestingly, PEDOT:PSS also appears to exhibit a ferroelectric-like loop when considering only the off-field piezoelectric response. However, the analysis of the on-field loops provides further insight. Both materials show elongated

https://doi.org/10.1021/acsomega.6c01080
ACS Omega XXXX, XXX, XXX−XXX

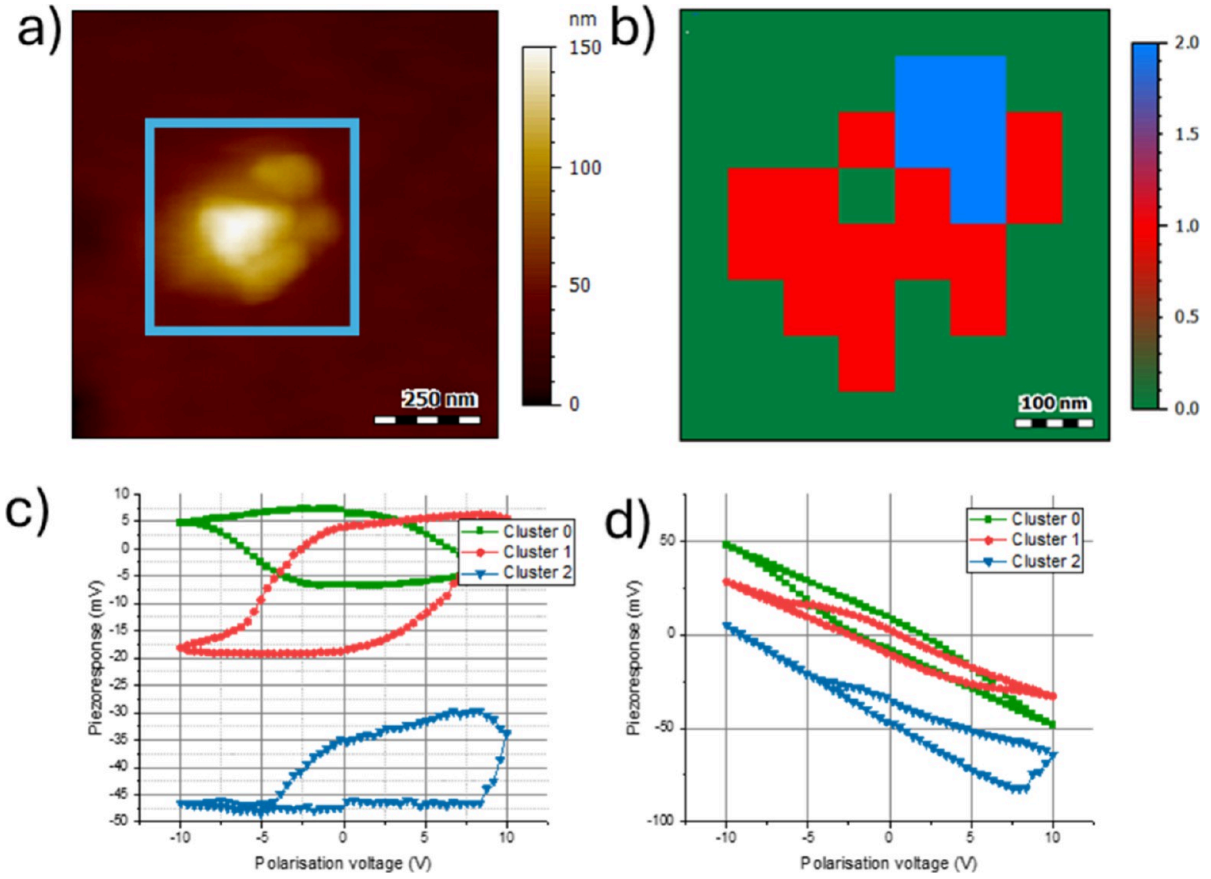

Figure 9. (a) Topography of a BFO aggregate in the PVDF-TrFE matrix. The blue square marks the ssPFM mapping region (8 × 8 curves over 500 × 500 nm). (b) PyssPFM clustering for k = 2. (c) Mean off-field piezoresponse loop. (d) Mean on-field piezoresponse loop.

loops indicative of strong electrostatic contributions (Figure 7c). Nevertheless, a pronounced shrinking of the loop between on-field and off-field conditions is observed for PEDOT:PSS. This behavior is consistent with previous reports,[64] where nonferroelectric materials may exhibit apparent ferroelectric-like loops due to electrostatic artifacts. The strong reduction of the piezoresponse between on- and off-field conditions is therefore used here as a criterion to identify nonferroelectric behavior.

Furthermore, analysis of individual point measurements within the PEDOT:PSS region reveals a complete disappearance of hysteresis in amplitude, phase, and piezoresponse signals (Figure S21a−d). The slight opening observed in the mean on-field loop of cluster 0 is attributed to the averaging process and to imperfect clustering, which may include a small contribution from BFO regions.

Increasing the number of clusters reveals additional complexity within the BFO phase (Figure 8). A main cluster similar to the initial one and a second cluster exhibiting an off-centered response were observed. This second cluster is likely associated with particles exhibiting unfavorable crystallographic orientations or partial coating by PEDOT:PSS, which can hinder the polarization switching within the accessible voltage range.

At first glance, the piezoresponse loops of this second cluster may suggest a phase-calibration artifact. However, analysis of single-point measurements in these regions shows a stable phase signal without inversion, while the amplitude exhibits an open, non-butterfly-like response, likely due to a limited polarization range (Figure S21h−j). The corresponding phase images acquired before and after ssPFM measurements (Figure S22a,b) confirm the absence of phase inversion, consistent with nonswitchable behavior. Statistical analysis further reveals a relatively narrow distribution of coercive fields for cluster 1 and a broader distribution for cluster 2 (Figure S22c,d).

For the hybrid ferroelectric nanocomposite (Figure 9), the ferroelectric response distribution became more distinct. The two components can be clearly identified on the basis of the orientation of their hysteresis loops. The polymer exhibits a counterclockwise loop orientation (cluster 0), consistent with a negative piezoelectric coefficient, while the inorganic component displays a clockwise loop orientation (cluster 1), indicative of a positive piezoelectric coefficient. The on-field loops retain a pinched shape characteristic of electrostatic contributions while preserving clear hysteresis behavior in both cases.

A third population (cluster 2) is identified within BFO aggregates, characterized by off-centered loops with strong piezoresponse amplitude but no phase inversion under an applied field (Figure S23). These regions exhibit non-switchable yet electromechanically active behavior, observed across multiple grains in the composite. The orientation of this fixed piezoresponse is directly correlated with the local phase orientation.

Importantly, these nonswitchable regions do not show a clear correlation with particle size, as particles of similar apparent dimensions (100−200 nm) may exhibit either switchable or nonswitchable behavior. This suggests that the

https://doi.org/10.1021/acsomega.6c01080
ACS Omega XXXX, XXX, XXX−XXX

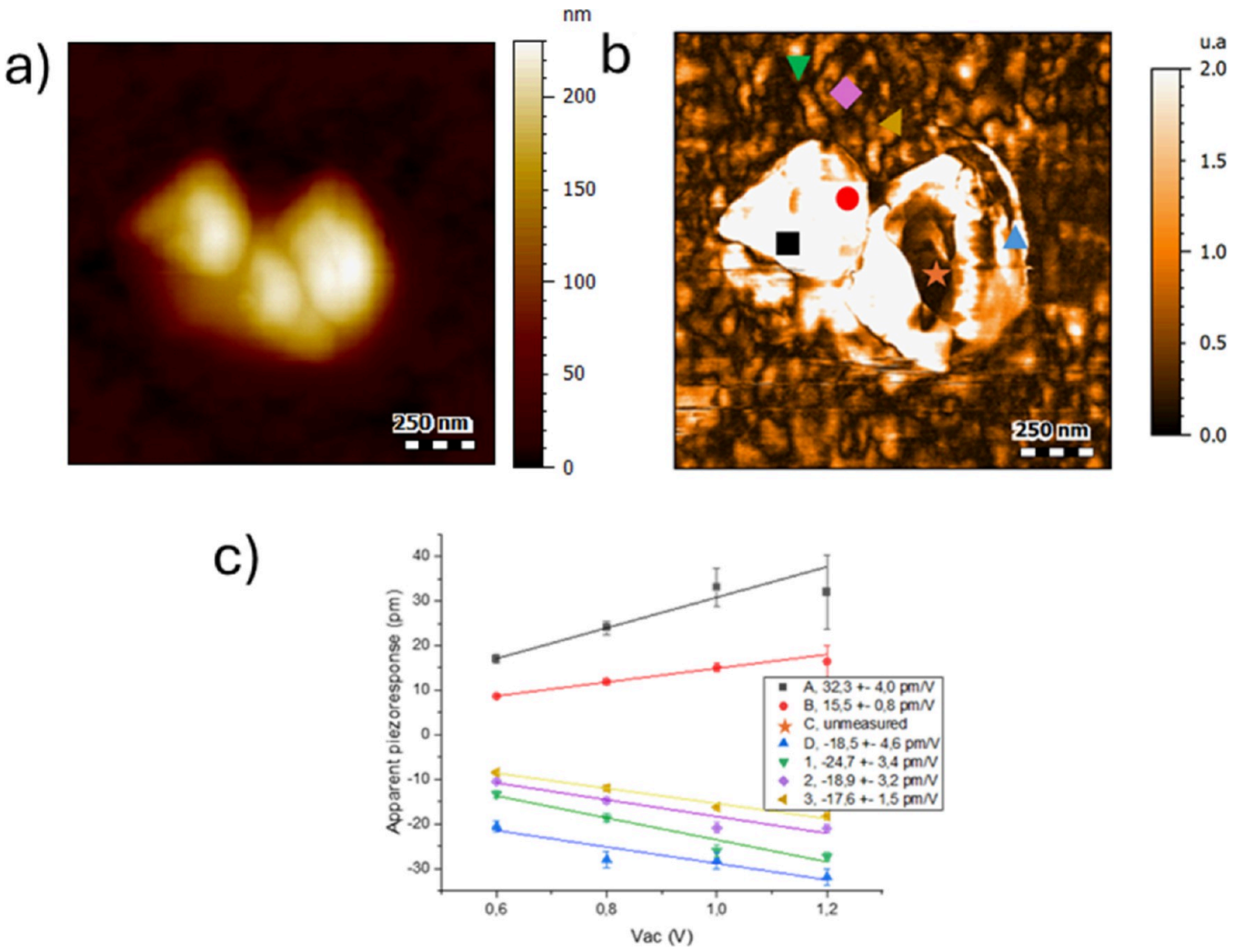

Figure 10. DFRT-PFM imaging of a multigrain BFO aggregate embedded in PVDF−TrFE. Vertical mode (250−350 kHz): (a) topography and (b) amplitude. (c) Apparent piezoresponse as a function of V_{ac} at all locations highlighted in (b).

phenomenon is not solely governed by size effects. A more plausible explanation involves local electrical boundary conditions, including incomplete electrical coupling to the bottom electrode and dielectric screening effects induced by the PVDF-TrFE matrix, which may locally reduce the effective electric field. The possible presence of secondary nonferroelectric phases in BFO may also contribute, although the persistence of a strong piezoresponse suggests that this is not the dominant mechanism.

Usually, ssPFM studies are performed at a single location,[67−69] providing a global assessment of ferroelectric response. In contrast, relatively few studies exploit the cartographic capabilities of ssPFM.[70] In nanocomposite systems, it is also common to report only a single representative loop per component.[38,42] In this work, the use of PyssPFM enables spatially resolved mapping of ferroelectric behavior over extended areas, allowing the identification of local variations within a complex heterostructure (Figures S22 and S24).

Although the comparison between on-field and off-field mean loops provides a useful indicator of ferroelectric behavior, the averaging process may reduce sensitivity to local variations. Therefore, local comparisons of amplitude and phase images before and after switching are used as a more robust criterion, showing clear hysteresis preservation in BFO and PVDF-TrFE regions, despite the presence of electrostatic contributions.

Finally, complementary cKPFM measurements are used to confirm the ferroelectric nature of the signal (Figure S25). In both PVDF-TrFE and switchable BFO regions, two stable states are observed at the two extreme of reading voltage, consistent with ferroelectric bistability (Figure S25b,c), similar to reference PZT samples (Figure S9c). In contrast, nonswitchable BFO regions exhibit a single stable state, distinguishing them from nonferroelectric materials, which typically show a linear response (Figure S9d). This indicates that these regions are likely ferroelectric but require higher electric fields to achieve polarization switching within the explored voltage range.

3.5. Local d_{33}^{app} Evaluation

Evaluation of the local d_{33}^{app} on the nanocomposite samples is illustrated in Figure 10. All measurements are performed after a local poling. The apparent piezoelectric coefficients in the polymer matrix are consistent with one another, with a mean value of around −20.2 pm/V, as expected for this material.[71,72]

On the other hand, the BFO aggregates present a wide range of responses, from no response to up to 34.4 pm/V. Some

https://doi.org/10.1021/acsomega.6c01080
ACS Omega XXXX, XXX, XXX−XXX

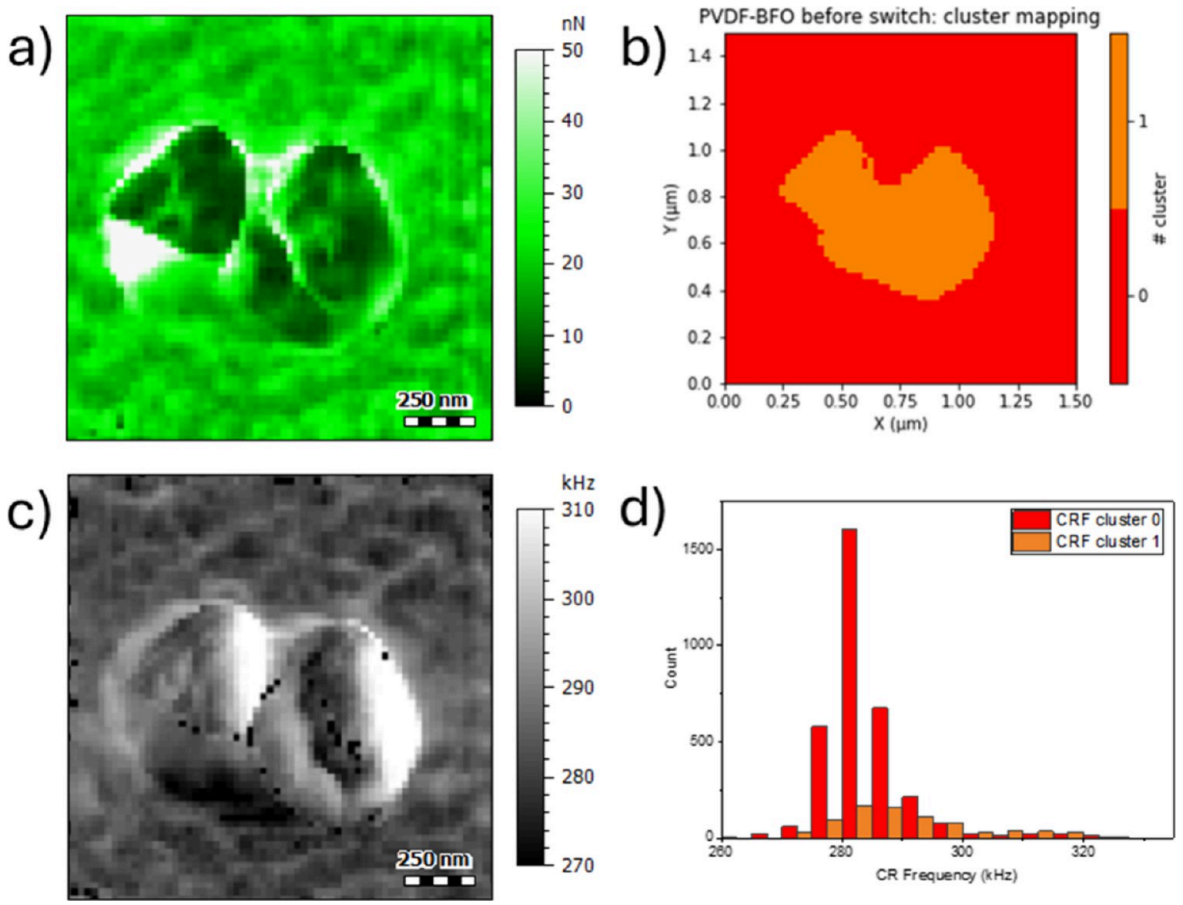

Figure 11. (a) Adhesion mapping associated with the DataCube-PFM measurement of a multigrain BFO aggregate embedded in PVDF−TrFE in pristine state. (b) Clustering map (K = 2). (c) CR frequency map. (d) Corresponding frequency histograms.

areas present negative d_{33}^{app}, −18.5 pm/V. Analysis of the postpolarization phase images, after calibration, indicates that these negative d_{33}^{app} values are associated with a nonpolarizable area of the aggregates and with a negative phase orientation (Figure S26). The dispersity of responses most likely arises from the random orientation of the BFO particles as no alignment procedure was performed. As a consequence, the projection of the polarization axis along the vertical measurement direction can vary locally, which may naturally lead to a broad distribution of the apparent piezoelectric coefficients.

From those results, it emerges that single-position measurements are not recommended for measuring local d_{33}^{app} on such samples. It is recommended to map the spectroscopic response of the nanocomposites.

The d_{33}^{app} range of measurements on polarized BFO particles is between 10 and 40 pm/V whether in the PVDF-TrFE matrix or in PEDOT:PSS in our study. Compared to bulk BFO materials, our values appear relatively underestimated (45−50 pm/V).[73] However, it has been reported that direct comparison with bulk material responses should be avoided because the response tends to change with the shrinking of the material.[74] Furthermore, additional carefulness is recommended. Several studies present relatively high piezoelectric coefficients between 60 and 80 pm/V but collected only with on-field measurements identifiable by the characteristic "pinched" shape and lack of saturation of their piezo loops. It strongly undermines their reliability.[75,76] More consistent studies including those combining direct and indirect PFM measurements[50] and theoretical predictions[77] place the intrinsic coefficient of BFO particles closer to 20−40 pm/V,[78] as we observe.

3.6. DataCube-PFM Mapping

DataCube-PFM mapping of the same region of the ferroelectric nanocomposite in its pristine state presented in Figure 5 is presented in Figures 11 and 12. DataCube measurements are based on the collection of force curves. They give access to mechanical properties, such as adhesion. This property is visibly different between both components of the composites (Figure 11 and Figure S18b). This distinction is used as the basis for data clustering with the PyCAROS software from our lab (Figure 11b). Using the latter on the CR frequency mapping, it appears that those have a relatively large distribution of value for both components (Figure 11c). The frequency shows a shift of several dozen kHz on the particles. This is consistent with the rough topography. The uniform matrix also presents kHz variation (Figure 11d).

The amplitude, phase, and amplification factor are extracted for each pixel from the SHO fit (Figure 12a−c), and the apparent surface displacement D is reconstructed from all these channels (Figure 12d). The polymer matrix shows a very weak surface displacement in its pristine state (Figure 12e), and the particles present a wide range of responses (Figure 12f). The central right region of the aggregate is unresponsive, and the rest of this part shows a negative pristine response. Left: Positive orientation.

Apparent surface displacement D is reconstructed after a local polarization at +10 V from the same parameters as before

https://doi.org/10.1021/acsomega.6c01080
ACS Omega XXXX, XXX, XXX−XXX

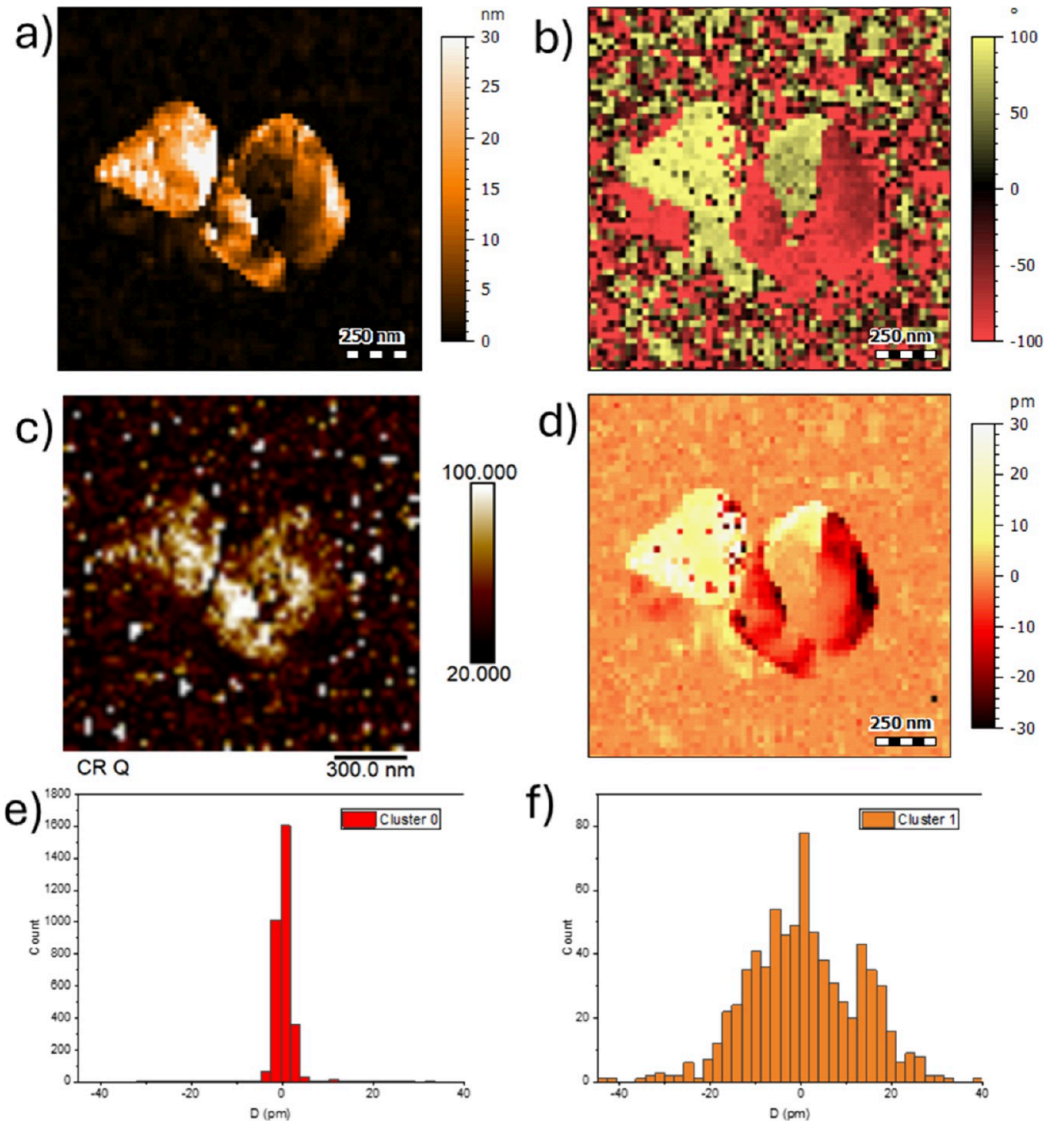

Figure 12. DataCube-PFM imaging of a multigrain BFO aggregate embedded in PVDF−TrFE in pristine state. (a) Amplitude, (b) phase, (c) *Q*-factor. (d) Reconstructed apparent surface displacement *D*. Histograms of *D* for clustered regions: (e) cluster 0 and (f) cluster 1 (unpoled state).

(Figure 13a−d). The matrix shows a global uniformization of its responses in every DataCube channel, resulting in a global decrease of its apparent surface displacement to a value around 20 pm (Figure 13e). This *D* value agrees with the measured d_{33}^{app} (Figure 10c). The particle aggregates show a partial reorientation, with some of the previously down area switching up (Figure 13b), with a global augmentation of the *D* value (Figure 13f). The nonresponsive central region stays nonresponsive. The rest of the cluster switches up, while a small region stays with a down orientation. This is the same area that showed a negative d_{33}^{app} (Figure 10c). The pointwise d_{33}^{app} value and polarized mapping show consistent values.

Another advantage of working in DataCube-PFM is the possibility to obtain quality PFM images on rough structures. The comparison of the DFRT image (Figure 6b,c) and DataCube-PFM one (Figure 12a,b) shows an identical ferroelectric domain structure in the matrix. For the domains on top of the particles, the phase image is far more stable in DataCube. There is no longer the phase overshoot and instability reported in DFRT-PFM. This arises from the force-curve aspect driving the measurement, allowing for a more stable approach. The main drawback is the acquisition time of the DataCube measurement. For a resolution four times lower than the DFRT images, the measurement in DataCube takes around 60 min, while the DFRT image only took 20 min.

4. CONCLUSIONS

BFO nanoparticles are successfully synthesized using a sol−gel method and are incorporated inside a PVDF-TrFE ferroelectric polymer matrix. The dominance of the rhombohedral ferroelectric phases was demonstrated by XRD. Thin films of nanocomposites were prepared using spin coating. The size and dispersion of BFO aggregates inside the nanocomposites were observed by SEM measurements.

Various PFM modes were used to investigate the piezo- and ferroelectric properties of the nanocomposite samples. The ferroelectric pristine structures of both parts are unveiled simultaneously through their mechanical disparities using DFRT-PFM, in both vertical and lateral modes.

The specific ferroelectric loop tendencies of the nanocomposites are investigated by PyssPFM mapping. The loop orientation identifies the nanocomposite constituents from

https://doi.org/10.1021/acsomega.6c01080
ACS Omega XXXX, XXX, XXX−XXX

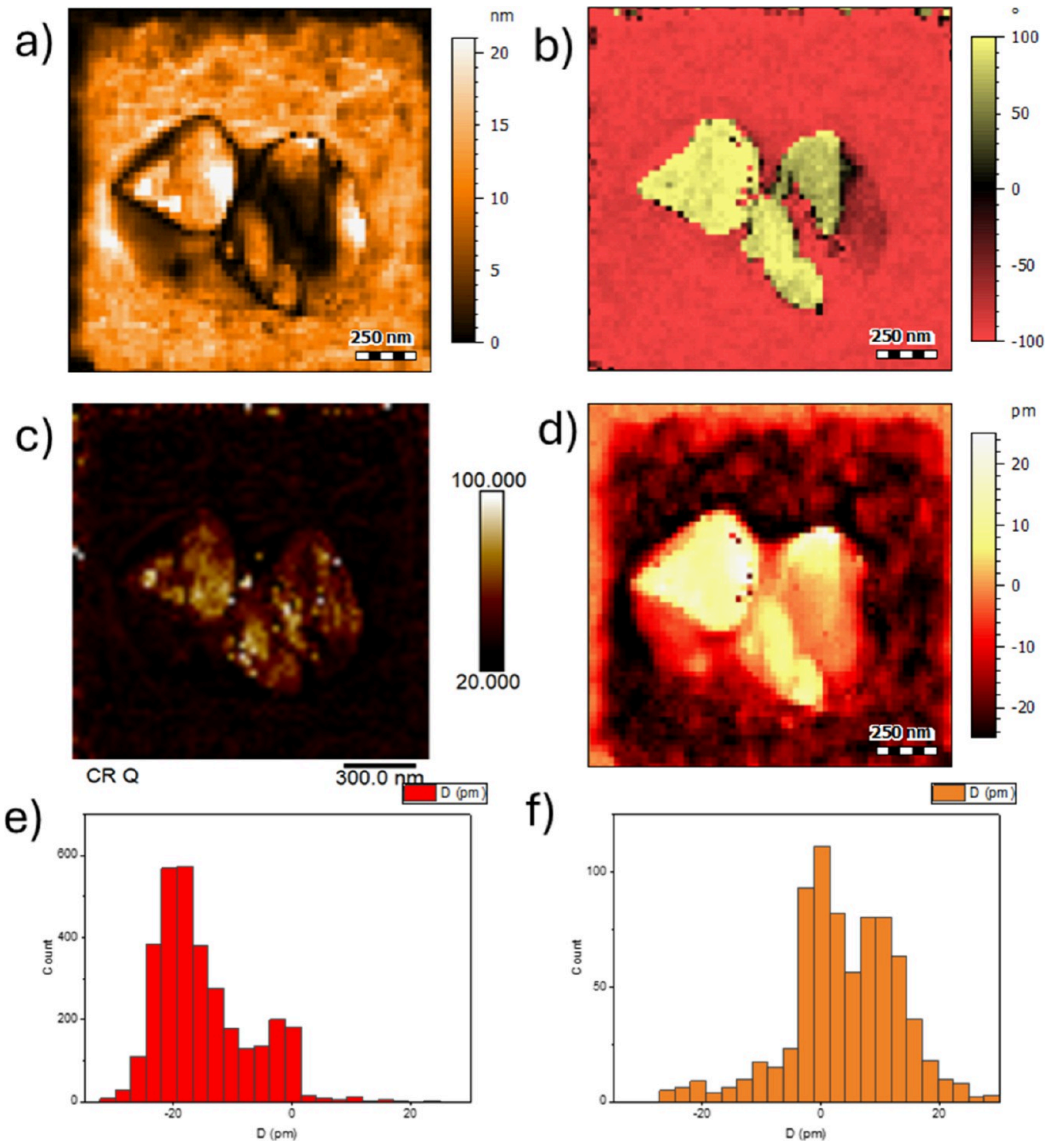

Figure 13. DataCube-PFM imaging of a multigrain BFO aggregate embedded in PVDF−TrFE after polarization at +10 V. (a) Amplitude, (b) phase, and (c) *Q*-factor. (d) Reconstructed apparent surface displacement *D*. Histograms of polarized D: (e) cluster 0 and (f) cluster 1.

their respective piezoelectric coefficient: a clockwise orientation for the perovskite phase and a counterclockwise orientation for the polymer. A third population emerges from the nanoparticles, corresponding to nonswitchable areas. This nonreversibility likely arises from the insulating characteristics of both present materials. Their local superposition prevents polarization in the studied voltage range.

Local evaluation of the apparent d_{33} presents a uniform response inside the polymer matrix with a mean value around −20 pm/V. BFO particles show a wider range of responses from 10 to 40 pm/V. Some unswitchable areas present a negative d_{33}^{app}.

Data cube PFM images are used to further investigate the d_{33}^{app} distribution by reconstruction of the local apparent surface displacement over an area where each pixel is a spectroscopic measurement. The *D* value distribution is consistent with the local d_{33}^{app} measurements. DataCube imaging proves to be an effective approach for analyzing PFM responses in complex 3D structures without the risk of phase overshoot and loss of stability.

In conclusion, this study explores different ways to assess piezo- and ferroelectric responses of complex nanostructured systems combining imaging, local spectroscopic, and imaging spectroscopic techniques. The complex and complete range of responses of hybrid ferroelectric nanomaterials is demonstrated for PVDF-TrFE/BFO nanocomposites. This work advances the understanding of ferroelectric behavior in nanocomposite systems and strengthens their potential for future technological applications.

■ ASSOCIATED CONTENT

Supporting Information

The Supporting Information is available free of charge at https://pubs.acs.org/doi/10.1021/acsomega.6c01080.

Raman spectroscopy of PVDF-TrFE and BFO; film thickness and nanomechanical characterization (PFT); AFM probe calibration; electrostatic blind spot (ESBS) optimization; phase offset correction; ssPFM measurement scheme; SHO fitting parameters; cKPFM methodology and reference measurements on ferroelectric and

https://doi.org/10.1021/acsomega.6c01080
ACS Omega XXXX, XXX, XXX−XXX

nonferroelectric samples; ZnO calibration and d_{33} determination; electron microscopy imaging; conductive AFM (c-AFM) measurements; summary of thickness, roughness, and BFO aggregate exposure; DFRT-PFM imaging; mechanical mapping (modulus and adhesion); DataCube-PFM analysis; ssPFM clustering and local hysteresis loop analysis; phase imaging and statistical analysis; cKPFM validation of switching behavior; and influence of film thickness on polarizability (PDF)

AUTHOR INFORMATION

Corresponding Author

Philippe Leclère − *Laboratory for Physics of Nanomaterials and Energy (LPNE), Research Institute in Materials Science and Engineering, University of Mons (UMONS), Mons B-7000, Belgium;* orcid.org/0000-0002-5490-0608; Email: philippe.leclere@umons.ac.be

Authors

Pierre Nickmilder − *Laboratory for Physics of Nanomaterials and Energy (LPNE), Research Institute in Materials Science and Engineering, University of Mons (UMONS), Mons B-7000, Belgium;* orcid.org/0009-0009-7101-151X

Sergio González Casal − *Laboratory for Physics of Nanomaterials and Energy (LPNE), Research Institute in Materials Science and Engineering, University of Mons (UMONS), Mons B-7000, Belgium*

Complete contact information is available at: https://pubs.acs.org/10.1021/acsomega.6c01080

Author Contributions

The manuscript was written through the contributions of all authors. All authors have approved the final version of the manuscript.

Funding

Research at LPNE (UMONS) is partly supported by F.R.S. FNRS (Belgium) via the Grands Equipements Project (40007941) − 2022 "Interuniversity Platform for the Analysis of the Nanoscale Properties of Emerging Materials and their Applications (IPANEMA)" and the F.R.S. FNRS PDR Program "PiezoFlexoTronics".

Notes

The authors declare no competing financial interest.

ACKNOWLEDGMENTS

The authors acknowledge the support provided by Prof Maurice Gonon from "Faculté Polytechnique de Mons" (FPMs) for his help on RX data collection and interpretation, and the help of Dr. Hugo Valloire from "Institut Matériaux Microélectronique Nanosciences de Provence" (im2np) at Aix-Marseille University (Marseille, France) for the ssPFM data analysis.

REFERENCES

(1) Babiker, D., Ciucci, M. *Renewable energy*, 2025. https://www.europarl.europa.eu/factsheets/en/sheet/70/energia-ze-zrodelodnawialnych.

(2) Wang, X. Piezoelectric nanogenerators—Harvesting ambient mechanical energy at the nanometer scale. *Nano Energy* **2012**, *1*, 13−24.

(3) Fan, F. R.; Tang, W.; Wang, Z. L. Flexible Nanogenerators for Energy Harvesting and Self-Powered Electronics. *Adv. Mater.* **2016**, *28*, 4283−4305.

(4) Briscoe, J.; Dunn, S. Piezoelectric nanogenerators − a review of nanostructured piezoelectric energy harvesters. *Nano Energy* **2015**, *14*, 15−29.

(5) Zhang, N.; Yokota, H.; Glazer, A. M.; Ren, Z.; Keen, D. A.; Keeble, D. S.; Thomas, P. A.; Ye, Z.-G. The missing boundary in the phase diagram of PbZr1−xTixO3. *Nat. Commun.* **2014**, *5*, 5231.

(6) Zhang, Y.; Kim, H.; Wang, Q.; Jo, W.; Kingon, A. I.; Kim, S.-H.; Jeong, C. K. Progress in lead-free piezoelectric nanofiller materials and related composite nanogenerator devices. *Nanoscale Adv.* **2020**, *2*, 3131−3149.

(7) Aksel, E.; Jones, J. L. Advances in Lead-Free Piezoelectric Materials for Sensors and Actuators. *Sensors* **2010**, *10*, 1935−1954.

(8) Wu, J.; Fan, Z.; Xiao, D.; Zhu, J.; Wang, J. Multiferroic bismuth ferrite-based materials for multifunctional applications: Ceramic bulks, thin films and nanostructures. *Prog. Mater. Sci.* **2016**, *84*, 335−402.

(9) Catalan, G.; Scott, J. F. Physics and Applications of Bismuth Ferrite. *Adv. Mater.* **2009**, *21*, 2463−2485.

(10) Liu, X.; Peng, Y.; Zhang, F.; Sun, T.; Peng, Y.; Wen, L.; Li, H. Enhanced performance of flexible BiFeO3 ferroelectric memory with Mica substrate via SrTiO3 buffer layer. *Sci. Rep* **2024**, *14*, 25292.

(11) Khorsand Zak, A.; Hashim, A. M. Recent advances in $BiFeO_3$-based nanostructures: Properties and applications. *Coord. Chem. Rev.* **2025**, *523*, No. 216297.

(12) Wang, N.; Luo, X.; Han, L.; Zhang, Z.; Zhang, R.; Olin, H.; Yang, Y. Structure, Performance, and Application of BiFeO3 Nanomaterials. *Nano-Micro Lett.* **2020**, *12*, 81.

(13) Kong, L. B.; Zhang, T. S.; Ma, J.; Boey, F. Progress in synthesis of ferroelectric ceramic materials via high-energy mechanochemical technique. *Prog. Mater. Sci.* **2008**, *53*, 207−322.

(14) Teixeira, G. F., Lustosa, G. M., Zanetti, S. M., Zaghete, M. A., Chemical synthesis and epitaxial growth methods for the preparation of ferroelectric ceramics and thin films. In *Magnetic, Ferroelectric, and Multiferroic Metal Oxides*; Elsevier, 2018: pp 121−137. .

(15) Beigh, N. T.; Mallick, D. Low-Cost, High-Performance Piezoelectric Nanocomposite for Mechanical Energy Harvesting. *IEEE Sensors J.* **2021**, *21*, 21268−21276.

(16) Petrukhin, D.; Salnikov, V.; Nikitin, A.; Sidane, I.; Slimani, S.; Alberti, S.; Peddis, D.; Omelyanchik, A.; Rodionova, V. Effect of Bismuth Ferrite Nanoparticles on Physicochemical Properties of Polyvinylidene Fluoride-Based Nanocomposites. *J. Compos. Sci.* **2024**, *8*, 329.

(17) Nambiar, R. B.; Perumal, A. B.; Sadiku, E. R. Advances in Nanocomposites: Preparation, Characterization, Properties, and Applications. *Molecules* **2024**, *29*, 5924.

(18) Yang, R.; Li, J.; Wang, Y.; Liu, Y.; Du, X.; Li, W. Pyroelectric polyvinylidene fluoride film prepared by a novel combining method and its application in fully flexible infrared detector. *Infrared Physics & Technology* **2021**, *113*, No. 103624.

(19) Sinelnikov, A. N.; Melnikov, A. R.; Getmanov, Y. V.; Kolomeec, D. A.; Kalneus, E. V.; Fedin, M. V.; Veber, S. L. Temperature Dependence of the Sensitivity of PVDF Pyroelectric Sensors to THz Radiation: Towards Cryogenic Applications. *Sensors* **2024**, *24*, 5808.

(20) Saxena, P.; Shukla, P. A comprehensive review on fundamental properties and applications of poly(vinylidene fluoride) (PVDF). *Adv. Compos Hybrid Mater.* **2021**, *4*, 8−26.

(21) Rana, D. K.; Kundu, S. K.; Choudhary, R. J.; Basu, S. Enhancement of electrical and magnetodielectric properties of $BiFeO_3$ incorporated PVDF flexible nanocomposite films. *Mater. Res. Express* **2019**, *6*, No. 0850d9.

(22) Wang, Z.; Ye, J.; Liu, S.; Zhang, X.; Hou, Y.; Li, X.; Wang, H. Enhanced energy storage capability of hydroxylated BiFeO3/PVDF composites designed by compositionally gradient multilayer structures. *J. Alloys Compd.* **2025**, *1010*, No. 177194.

(23) Bae, J.-H.; Chang, S.-H. PVDF-based ferroelectric polymers and dielectric elastomers for sensor and actuator applications: a review. *Funct. Compos. Struct.* **2019**, *1*, No. 012003.

https://doi.org/10.1021/acsomega.6c01080
ACS Omega XXXX, XXX, XXX−XXX

(24) Bhadra, D.; Masud, Md.G.; Sarkar, S.; Sannigrahi, J.; De, S. K.; Chaudhuri, B. K. Synthesis of PVDF/$BiFeO_3$ nanocomposite and observation of enhanced electrical conductivity and low-loss dielectric permittivity at percolation threshold. *J. Polym. Sci. B Polym. Phys.* **2012**, *50*, 572−579.
(25) Rabadanova, A. A.; Selimov, D. A.; Shuaibov, A. O.; Alikhanov, N.M.-R.; Suleymanov, FIGURE S; Shishov, A. Y.; Salnikov, V. D.; Sangamesha, M. A.; Giraev, K. M.; Bamatov, I. M.; Orudzhev, F. F. Smart multi-stimuli responsive magneto-piezoelectric composite material based on PVDF and BiFeO3 nanoparticles for catalysis and energy harvesting. *Polymer* **2025**, *324*, No. 128241.
(26) Zhang, H.; Zhao, G.; Ma, S.; Zhang, B. Development of La-Doped $BiFeO_3$ /PVDF Nanocomposite Triboelectric Nanogenerator for Self-Powered Anticorrosion System. *ChemistrySelect* **2025**, *10*, No. e02906.
(27) Wu, Y.; Zhang, H.; Xu, Y.; Tang, Z.; Li, Z. Ferroelectric BiFeO3 modified PVDF-based electrolytes for high-performance lithium metal batteries. *J. Mater. Chem. A* **2024**, *12*, 20403−20413.
(28) Hu, X.; Che, Y.; Zhang, Z.; Shen, Q.-D.; Chu, B. $BiFeO_3$ − $BaTiO_3$ /P(VDF-TrFE) Multifunctional Polymer Nanocomposites. *ACS Appl. Electron. Mater.* **2021**, *3*, 743−751.
(29) Orudzhev, F.; Alikhanov, N.; Amirov, A.; Rabadanova, A.; Selimov, D.; Shuaibov, A.; Gulakhmedov, R.; Abdurakhmanov, M.; Magomedova, A.; Ramazanov, S.; Sobola, D.; Giraev, K.; Amirov, A.; Rabadanov, K.; Gadzhimagomedov, S.; Murtazali, R.; Rodionova, V. Porous Hybrid PVDF/BiFeO3 Smart Composite with Magnetic, Piezophotocatalytic, and Light-Emission Properties. *Catalysts* **2023**, *13*, 874.
(30) Yang, L.; Nickmilder, P.; Verhoogt, H.; Hoeks, T.; Leclère, P. Probing Viscoelastic Properties and Interfaces in High-Density Polyethylene Vitrimers at the Nanoscale Using Dynamic Mode Atomic Force Microscopy. *ACS Appl. Mater. Interfaces* **2024**, *16*, 38501−38510.
(31) Seychal, G.; Nickmilder, P.; Lemaur, V.; Ocando, C.; Grignard, B.; Leclère, P.; Detrembleur, C.; Lazzaroni, R.; Sardon, H.; Aranburu, N.; Raquez, J.-M. A novel approach to design structural natural fiber composites from sustainable CO 2 -derived polyhydroxyurethane thermosets with outstanding properties and circular features. *Composites Part A: Applied Science and Manufacturing* **2024**, *185*, No. 108311.
(32) Benstetter, G.; Hofer, G.; Liu, D.; Frammelsberger, W.; Lanza, M., Fundamentals of CAFM Operation Modes In *Conductive Atomic Force Microscopy*; John Wiley & Sons, Ltd, 2017: pp 45−77. .
(33) Pham, S. H.; Ferri, A.; Da Costa, A.; Mohan, M. M. S.; Tran, V. D.; Nguyen, D. C.; Viville, P.; Lazzaroni, R.; Desfeux, R.; Leclère, P. Nanoscale Electrical Investigation of Transparent Conductive Electrodes Based on Silver Nanowire Network. *Adv. Materials Inter* **2022**, *9*, No. 2200019.
(34) Magonov, S. Piezoresponse Force Microscopy in Its Applications. *N.-M. Development (n.d.)*, 2019, 14.
(35) Shen, C *Atomic Force Microscopy for Energy Research*; 1st ed., CRC Press: Boca Raton, 2022. .
(36) Ravisankar, M. S.; Rasi, U. P. M. Study of local piezo and ferroelectric characteristics of PVDF + Bi25FeO40 composite nanodots using piezoforce microscopy. *J. Mater. Sci: Mater. Electron* **2024**, *35*, 312.
(37) Cavallini, D., Fortunato, M., Bellis, G. D., Sarto, M. S., PFM Characterization of Piezoelectric PVDF/ZnONanorod thin films. In *2018 IEEE 18th International Conference on Nanotechnology (IEEE-NANO)*; IEEE: Cork, Ireland, 2018: pp 1−3. .
(38) Tran, V. D.; Truong, H.-C.; Nguyen, T. V.; Leclère, P.; Duong, T.-T.; Bui, T. H.; Nguyen, V. Q. Piezoelectric responses of PVDF-KBT electrospun nanocomposite fibres via nanoscale mapping. *Ceram. Int.* **2023**, *49*, 38288−38296.
(39) Magnani, A.; Capaccioli, S.; Azimi, B.; Danti, S.; Labardi, M. Local Piezoelectric Response of Polymer/Ceramic Nanocomposite Fibers. *Polymers* **2022**, *14*, 5379.
(40) Viehland, D.; Li, J. F.; Yang, Y.; Costanzo, T.; Yourdkhani, A.; Caruntu, G.; Zhou, P.; Zhang, T.; Li, T.; Gupta, A.; Popov, M.; Srinivasan, G. Tutorial: Product properties in multiferroic nano-composites. *J. Appl. Phys.* **2018**, *124*, No. 061101.
(41) Park, J.; Lee, M. H.; Kim, D. J.; Kim, M.-H.; Kim, W.-J.; Do, D.; Jeon, J. H.; Park, B. H.; Song, T. K. High piezoelectric performance of lead-free $BiFeO_3$ − $BaTiO_3$ thin films grown by a pulsed laser deposition method. *RSC Adv.* **2016**, *6*, 106899−106903.
(42) Baji, A.; Mai, Y.-W.; Li, Q.; Liu, Y. Nanoscale investigation of ferroelectric properties in electrospun barium titanate/polyvinylidene fluoride composite fibers using piezoresponse force microscopy. *Compos. Sci. Technol.* **2011**, *71*, 1435−1440.
(43) Liu, X.; Kuang, X.; Xu, S.; Wang, X. High-sensitivity piezoresponse force microscopy studies of single polyvinylidene fluoride nanofibers. *Mater. Lett.* **2017**, *191*, 189−192.
(44) Seol, D.; Kim, B.; Kim, Y. Non-piezoelectric effects in piezoresponse force microscopy. *Curr. Appl. Phys.* **2017**, *17*, 661−674.
(45) Killgore, J. P.; Robins, L.; Collins, L. A Universal Approach to Electrostatically-Blind Quantitative Piezoresponse Force Microscopy. *arXiv preprint arXiv:2112.09665*, **2021**.
(46) Fortunato, M.; Bidsorkhi, H. C.; Chandraiahgari, C. R.; De Bellis, G.; Sarto, F.; Sarto, M. S. PFM Characterization of PVDF Nanocomposite Films With Enhanced Piezoelectric Response. *IEEE Trans. Nanotechnology* **2018**, *17*, 955−961.
(47) Zhu, H.; Yang, Y.; Ren, W.; Niu, M.; Hu, W.; Ma, H.; Ouyang, J. Rhombohedral BiFeO3 thick films integrated on Si with a giant electric polarization and prominent piezoelectricity. *Acta Mater.* **2020**, *200*, 305−314.
(48) Wu, S.; Zhang, J.; Liu, X.; Lv, S.; Gao, R.; Cai, W.; Wang, F.; Fu, C. Micro-Area Ferroelectric, Piezoelectric and Conductive Properties of Single BiFeO3 Nanowire by Scanning Probe Microscopy. *Nanomaterials* **2019**, *9*, 190.
(49) Singh, H. H.; Khare, N. Improved performance of ferroelectric nanocomposite flexible film based triboelectric nanogenerator by controlling surface morphology, polarizability, and hydrophobicity. *Energy* **2019**, *178*, 765−771.
(50) Vila-Fungueiriño, J. M.; Gómez, A.; Antoja-Lleonart, J.; Gázquez, J.; Magén, C.; Noheda, B.; Carretero-Genevrier, A. Direct and converse piezoelectric responses at the nanoscale from epitaxial $BiFeO_3$ thin films grown by polymer assisted deposition. *Nanoscale* **2018**, *10*, 20155−20161.
(51) Jesse, S.; Baddorf, A. P.; Kalinin, S. V. Switching spectroscopy piezoresponse force microscopy of ferroelectric materials. *Appl. Phys. Lett.* **2006**, *88*, No. 062908.
(52) Valloire, H.; Quéméré, P.; Vaxelaire, N.; Kuentz, H.; Le Rhun, G.; Borowik, Ł. Enhancing ferroelectric characterization at nanoscale: A comprehensive approach for data processing in spectroscopic piezoresponse force microscopy. *J. Appl. Phys.* **2024**, *135*, No. 194101.
(53) Cui, A.; Wolf, P. D.; Ye, Y.; Hu, Z.; Dujardin, A.; Huang, Z.; Jiang, K.; Shang, L.; Ye, M.; Sun, H.; Chu, J. Probing electro-mechanical behaviors by datacube piezoresponse force microscopy in ambient and aqueous environments. *Nanotechnology* **2019**, *30*, No. 235701.
(54) Kim, J. K.; Kim, S. S.; Kim, W.-J. Sol−gel synthesis and properties of multiferroic BiFeO3. *Mater. Lett.* **2005**, *59*, 4006−4009.
(55) Arrigoni, A.; Brambilla, L.; Bertarelli, C.; Serra, G.; Tommasini, M.; Castiglioni, C. P(VDF-TrFE) nanofibers: structure of the ferroelectric and paraelectric phases through IR and Raman spectroscopies. *RSC Adv.* **2020**, *10*, 37779−37796.
(56) Seo, J.; Son, J. Y.; Kim, W.-H. Structural and ferroelectric properties of P(VDF-TrFE) thin films depending on the annealing temperature. *Mater. Lett.* **2019**, *238*, 294−297.
(57) Krutko, M.; Poling, H. M.; Sheth, M.; Kongsomros, S.; Bryan, A. E.; Sharma, M.; Singh, A.; Reza, H. A.; Wikenheiser-Brokamp, K. A.; Takebe, T.; Helmrath, M. A.; Harris, G. M.; Esfandiari, L. Thermal Annealing Enhances Piezoelectricity and Regenerative Potential of PVDF-TrFE Nanofiber Scaffolds. *Adv. Materials Technologies* **2025**, *10*, No. e01513.
(58) Carter, J. L.; Kelly, C. A.; Jenkins, M. J. Processing optimization of PEDOT:PSS and PEDOT:PSS/Tween 80 films. *Polym. J.* **2023**, *55*, 253−260.

https://doi.org/10.1021/acsomega.6c01080
ACS Omega XXXX, XXX, XXX−XXX

(59) Soergel, E. Piezoresponse force microscopy (PFM). *J. Phys. D: Appl. Phys.* **2011**, *44*, No. 464003.
(60) Friedrich, S.; Cappella, B. Application of contact-resonance AFM methods to polymer samples. *Beilstein J. Nanotechnol.* **2020**, *11*, 1714−1727.
(61) Neumayer, S. M.; Saremi, S.; Martin, L. W.; Collins, L.; Tselev, A.; Jesse, S.; Kalinin, S. V.; Balke, N. Piezoresponse amplitude and phase quantified for electromechanical characterization. *J. Appl. Phys.* **2020**, *128*, No. 171105.
(62) Rodriguez, B. J.; Callahan, C.; Kalinin, S. V.; Proksch, R. Dual-frequency resonance-tracking atomic force microscopy. *Nanotechnology* **2007**, *18*, No. 475504.
(63) Balke, N.; Maksymovych, P.; Jesse, S.; Herklotz, A.; Tselev, A.; Eom, C.-B.; Kravchenko, I. I.; Yu, P.; Kalinin, S. V. Differentiating Ferroelectric and Nonferroelectric Electromechanical Effects with Scanning Probe Microscopy. *ACS Nano* **2015**, *9*, 6484−6492.
(64) Vasudevan, R. K.; Balke, N.; Maksymovych, P.; Jesse, S.; Kalinin, S. V. Ferroelectric or non-ferroelectric: Why so many materials exhibit "ferroelectricity" on the nanoscale. *Applied Physics Reviews* **2017**, *4*, No. 021302.
(65) Disnan, D.; Bacher, F.; Berger, S.; Schneider, M.; Schmid, U. Microstructural influence on thermal stability of ferroelectric properties in P(VDF-TrFE) spin cast thin films. *Polymer* **2024**, *298*, No. 126894.
(66) Sharma, P.; Wu, D.; Poddar, S.; Reece, T. J.; Ducharme, S.; Gruverman, A. Orientational imaging in polar polymers by piezoresponse force microscopy. *J. Appl. Phys.* **2011**, *110*, No. 052010.
(67) Tian, G.; Chen, D.; Fan, H.; Li, P.; Fan, Z.; Qin, M.; Zeng, M.; Dai, J.; Gao, X.; Liu, J.-M. Observation of Exotic Domain Structures in Ferroelectric Nanodot Arrays Fabricated via a Universal Nanopatterning Approach. *ACS Appl. Mater. Interfaces* **2017**, *9*, 37219−37226.
(68) Tian, G.; Chen, D.; Yao, J.; Luo, Q.; Fan, Z.; Zeng, M.; Zhang, Z.; Dai, J.; Gao, X.; Liu, J.-M. $BiFeO_3$ nanorings synthesized via AAO template-assisted pulsed laser deposition and ion beam etching. *RSC Adv.* **2017**, *7*, 41210−41216.
(69) Feng, K.; Liu, X.; Si, D.; Tang, X.; Xing, A.; Osada, M.; Xiao, P. Ferroelectric BaTiO 3 dipole induced charge transfer enhancement in dye-sensitized solar cells. *J. Power Sources* **2017**, *350*, 35−40.
(70) Jesse, S.; Rodriguez, B. J.; Choudhury, S.; Baddorf, A. P.; Vrejoiu, I.; Hesse, D.; Alexe, M.; Eliseev, E. A.; Morozovska, A. N.; Zhang, J.; Chen, L.-Q.; Kalinin, S. V. Direct imaging of the spatial and energy distribution of nucleation centres in ferroelectric materials. *Nat. Mater.* **2008**, *7*, 209−215.
(71) Hu, X.; You, M.; Yi, N.; Zhang, X.; Xiang, Y. Enhanced Piezoelectric Coefficient of PVDF-TrFE Films via In Situ Polarization. *Front. Energy Res.* **2021**, *9*, No. 621540.
(72) Piezoelectric Materials *P(VDF-TRFE) | Arkema Piezotech, (n.d.)*. https://piezotech.arkema.com/en/Products/piezoelectric-copolymers/ (accessed December 7, 2025).
(73) Tuluk, A.; Mahon, T.; Van Der Zwaag, S.; Groen, P. Estimating the true piezoelectric properties of BiFeO3 from measurements on BiFeO3-PVDF terpolymer composites. *J. Alloys Compd.* **2021**, *868*, No. 159186.
(74) Huan, Y.; Wang, X.; Fang, J.; Li, L. Grain size effect on piezoelectric and ferroelectric properties of BaTiO3 ceramics. *Journal of the European Ceramic Society* **2014**, *34*, 1445−1448.
(75) Shanthy, S.; Singh, S. K. MULTIFERROIC $BiFeO_3$ FILMS: CANDIDATE FOR ROOM TEMPERATURE MICRO BIOSENSOR. *Integr. Ferroelectr.* **2008**, *99*, 77−85.
(76) Wang, J.; Zheng, H.; Ma, Z.; Prasertchoung, S.; Wuttig, M.; Droopad, R.; Yu, J.; Eisenbeiser, K.; Ramesh, R. Epitaxial BiFeO3 thin films on Si. *Appl. Phys. Lett.* **2004**, *85*, 2574−2576.
(77) Graf, M.; Sepliarsky, M.; Machado, R.; Stachiotti, M. G. Dielectric and piezoelectric properties of BiFeO3 from molecular dynamics simulations. *Solid State Commun.* **2015**, *218*, 10−13.
(78) Amdouni, W.; Fricaudet, M.; Otoničar, M.; Garcia, V.; Fusil, S.; Kreisel, J.; Maghraoui-Meherzi, H.; Dkhil, B. $BiFeO_3$ Nanoparticles: The "Holy-Grail" of Piezo-Photocatalysts? *Adv. Mater.* **2023**, *35*, No. 2301841.

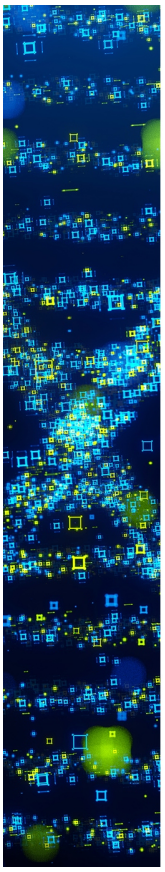

https://doi.org/10.1021/acsomega.6c01080
ACS Omega XXXX, XXX, XXX−XXX